***Supplementary Information to***

# Theranostic Near Infrared-Active Conjugated Polymer Nanoparticles

*Miao Zhao[1], Edward Leggett[1], Struan Bourke[1], Souzana Poursanidou[2], Sadie Carter-Searjeant[1], Steve Po[1], Marciano Palma do Carmo[1], Lea Ann Dailey[3], Philip Manning[4], Sean G. Ryan[5,6], Laura Urbano[2], Mark A. Green[1,]*, Aliaksandra Rakovich[1,]**

1. King's College London, Physics Department, Strand Building, London, WC2R 2LS, UK.

2. University of Hertfordshire, Department of Clinical, Pharmaceutical and Biological Sciences, College Lane, Hatfield, Hertfordshire, AL10 9AB, UK.

3. University of Vienna, Department of Pharmaceutical Technology and Biopharmacy, Vienna, Wien 1090, Austria.

4. Newcastle University, Translational and Clinical Research Institute, Faculty of Medical Sciences, Newcastle upon Tyne, Tyne and Wear, NE2 4HH, UK.

5. University of Hertfordshire, Department of Physics, Astronomy and Mathematics, College Lane, Hatfield, Hertfordshire, AL10 9AB, UK.

6. University College London, Centre for Advanced Biomedical Imaging, Gower Street, London, WC1E 6BT, UK.

# Contents

**Stabilities of bare and coated PTB7 CPNs**

Any application of the developed nanomaterials for photodynamic therapy would require storage for prolonged periods of time, utilization in physiological conditions and under prolonged excitations. Here we explore the stabilities of the prepared PTB7 CPN samples under such conditions.

***Stability under physiological conditions (in vitro)***

The stability of PTB7 CPN samples under physiological conditions was evaluated *in vitro* by monitoring the properties of the CPNs in solutions of different pH values and in the presence of Fetal Bovine Serum (FBS).

The stability of PTB7 samples in the presence of FBS was evaluated by monitoring their optical properties when dissolved in solutions of different FBS concentrations. Samples were excited at 620 nm, and the fluorescence spectra were recorded in the 640 – 900 nm spectral range. Results showed that the fluorescence intensity of the bare PTB7 and PTB7@F127 CPNs remained approximately the same across the investigated range of FBS concentrations (0-95 %v/v). For PTB7@PSMA CPNs sample, however, the fluorescence intensity increased sharply with increasing FBS concentrations, becoming stable at FBS concentrations higher than 50 %v/v (Figure S1.1a). For all samples and FBS

concentrations, the fluorescence peak fluctuated very little: a 4 nm and 6 nm shift was observed for PTB7@F127 CPNs and for PTB7@PSMA CPNs and bare PTB7 samples respectively (Figure S1.1b), all of which are much smaller than the full-width half-maximum of the peak (150-200 nm). Therefore, for PTB7@F127 CPNs and bare PTB7 samples, fluorescence appeared to be stable in the presence of different concentrations of FBS. For PTB7@PSMA CPN samples, the increase in the intensity of the fluorescence without major changes to the shape of the fluorescence bands indicates that the nature of the excitonic species responsible for the emission has not changed, but the interactions of the capping PSMA molecules with the core PTB7 chains is affected by the presence of the FBS. The result of these interactions seems to be reduced quenching of PTB7 fluorescence by the PSMA and a corresponding increase of the fluorescence intensity.

The different fluorescence behaviors of the three types of particles in FBS seem to suggest that the smaller PSMA copolymer molecules are affected the most by the presence of the FBS, implying possible changes to the physical packing of the polymer strands and/or organization of the copolymer molecules on the PTB7 core within the PTB7@PSMA CPNs, but not for the other two particles. Dynamic Light Scattering measurements were therefore performed to seek evidence for such reorganization. As can be seen in panels (c) and (d) of Figure S1.1, these data do support the hypothesis to some degree, as the largest changes in particle size were observed for the PTB7@PSMA CPNs. However, the hydrodynamic diameter of CPNs increased for all three samples at higher FBS concentrations: the average diameter of bare PTB7 CPNs increased from 211 nm to 370 nm, that of PTB7@F127 CPNs increased from 224 nm to 301 nm and that of the PTB7@PSMA CPNs increased from 164 to 410 nm. This corresponds to relative increases of 1.8, 2.5 and 1.4 in the average particle size of bare PTB7, PTB7@PSMA and PTB7@F127 CPNs. The DLS measurements presented here

clearly evidence the organization of polymer chains in the CPNs when in the presence of the FBS, but they do so for all three particles. It can be argued that the larger increase in particle size of the PTB7@PSMA CPNs is due to the stronger reorganization of the cap molecules, which would be in line with the observed changes in the fluorescence. However, further investigations into the photophysics of the PTB7 CPNs in FBS are required to make concrete conclusions in this regard.

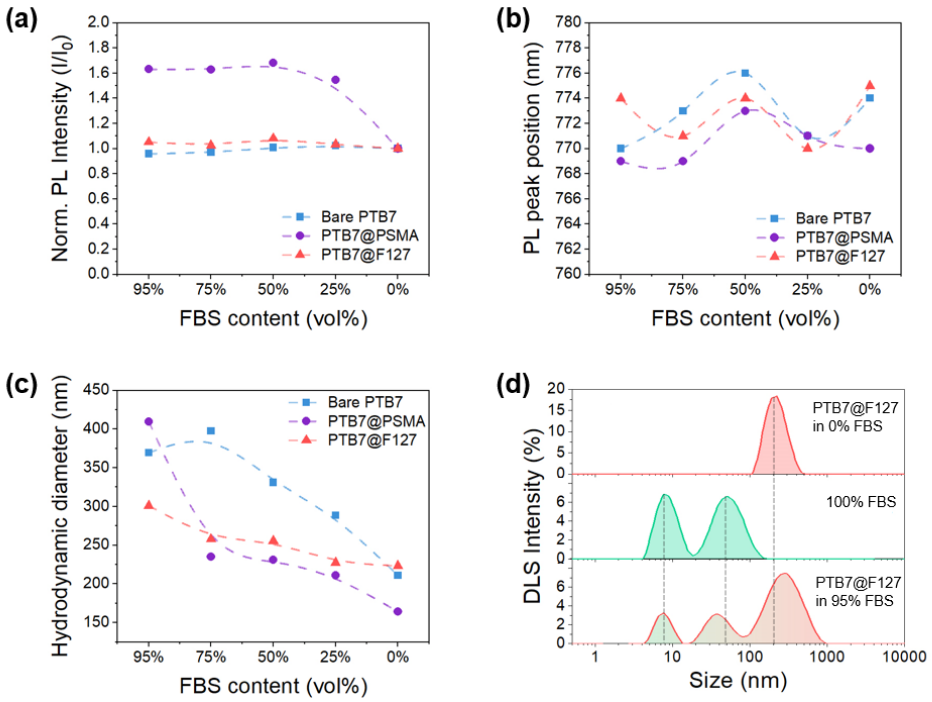


**Figure S1.1. Fluorescence and size of PTB7 samples in presence of different concentrations of FBS.** Both the intensity (a) and the position (b) of the fluorescence peak of all three PTB7 samples depended on the concentration of FBS. In panel (c), the size of all three PTB7 samples increased with increased concentration of FBS in solution and the size of PTB7@F127 is the mostly stable while the size of PTB7@PSMA CPNs increased the most obvious. In panel (d), the dashed violet line indicates the average size ($Z_{av}$) of the PTB7@F127 with 0% FBS in solution and the dashed olive line indicates the $Z_{av}$ of pure FBS.

The performance of CPNs in solutions of different pHs was evaluated next. Results showed that all samples performed best at normal physiological conditions (pH 7.4), with highest fluorescence QYs recorded for all three samples in this pH region (Figure S1.2a). Equally, the fluorescence QY of all three samples decreased sharply, capping-dependent but by no more than 50%, for pH values corresponding to tumor pathology (pH 5-7).[1,2] Associated with this decrease was also a blue shift of the fluorescence peak of the order of 6 nm for all three samples (Figure S1.2b), but again this is minimal compared to the FWHM of the fluorescence peaks. Nonetheless, the pH-sensitive fluorescence intensity properties of our theranostic CPNs probes could be of significance for differentiation of healthy and tumorous tissues.

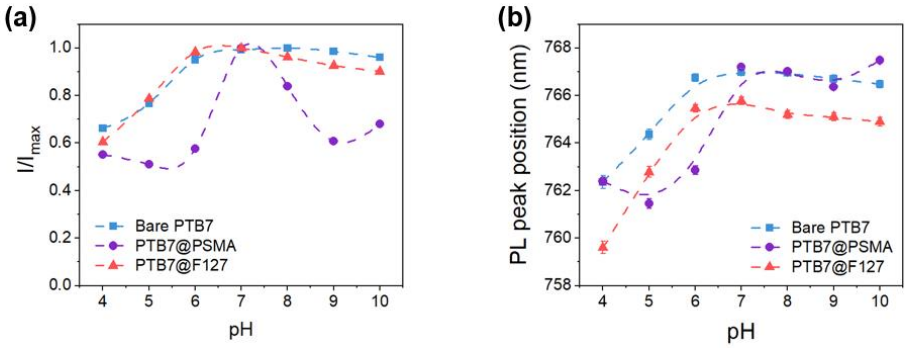


**Figure S1.2. Fluorescence of PTB7 samples in solutions of different pH values.** Both the intensity **(a)** and the position **(b)** of the fluorescence peak of all three PTB7 samples depended on the pH of the solution.

Dynamic light scattering measurements revealed that the hydrodynamic sizes of the bare PTB7 and PTB7@F127 CPNs remain approximately same across the investigated pH range (4-10, Figure S1.3a), and this was in line with the UV-vis measurements that showed minimal changes in the absorption spectra of these samples (Figure S1.3b and d). For PTB7@PSMA CPNs, however, notable

changes were observed both in the average hydrodynamic size of the CPNs and their absorption spectra (Figure S1.3a and c).

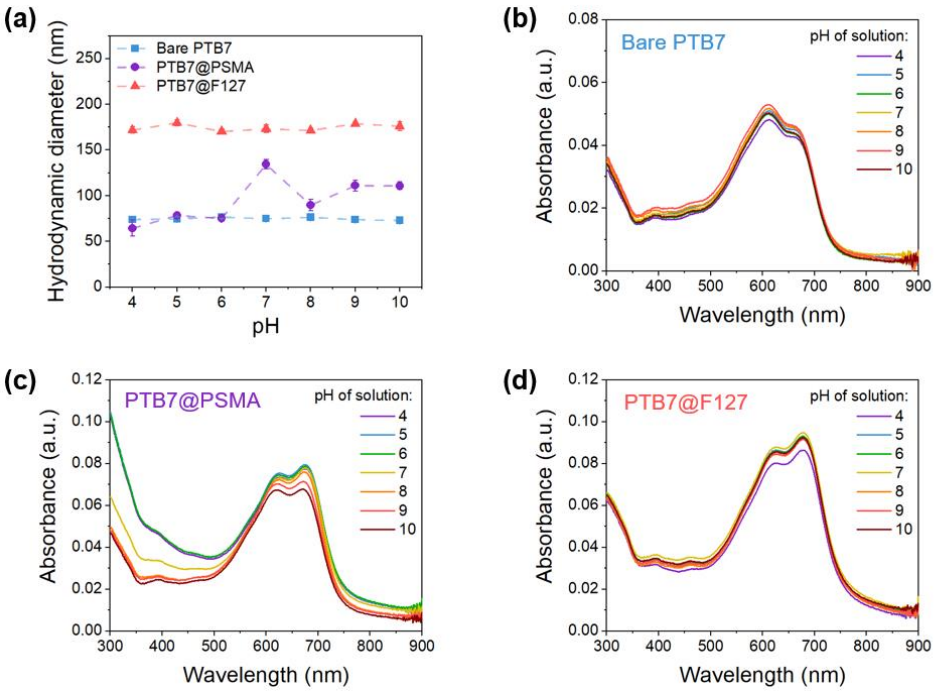


**Figure S1.3. Absorption and size of PTB7 CPNs as a function of pH.** (a) Average hydrodynamic diameter of bare PTB7 (blue), PTB7@PSMA CPNs (purple) and PTB7@F127 CPNs (pink) when dispersed in solutions of different pHs. Panels (b)-(d) show the pH dependency of the absorption spectra of (b) bare PTB7, (c) PTB7@PSMA CPNs and (d) PTB7@F127 CPNs.

The size of the particles decreased strongly when the pH of the solution was lowered (Figure S1.3a), with an associated increase in the absorption by these samples at the lower wavelength range (Figure S1.3c). In addition, above pH of 7.4, the relative intensities of the peaks corresponding to the two vibronic levels of the excited state of PTB7 polymer also changed, suggesting re-organization of the polymer in the CPNs. In general, it is reasonable that this would only occur for PTB7@PSMA CPNs as these particles have thin shells. For PTB7@F127 CPNs, the F127 copolymer is quite long and

therefore the energetic cost of restructuring is too high for it to occur. For base PTB7 CPNs, the relatively hydrophobic chains of PTB7 have already wrapped into the tightest core possible to minimize the surface energy; changing the pH of the solution does not change this energy significantly enough to cause a reorganization of the PTB7 chains. Therefore, for these two samples, the diameters remain approximately same under all pHs tested, while for PSMA coated CPNs, the reorganization of the PTB7 and copolymer chains led to changes in the CPNs diameter and changes of its absorbance.

***Photostability of CPN samples***

The photostability of the PTB7 CPN samples was investigated by monitoring the fluorescence signal under prolonged excitation. All PTB7 CPN samples showed some degree of photobleaching under continuous irradiation by the 635 nm CW laser, at 100μW power (Figure S1.4). However, for all of them, the photobleaching was relatively low: as shown in Figure S1.4, even after 2 hours of irradiation, the fluorescence intensity of PTB7 CPN samples decreased only by 25%. Therefore, the CPNs produced in this study demonstrate excellent photobleaching resistance and photochemical stable. This is critical for practical applications requiring long term imaging.

Even at higher excitation powers of 200 μW, the photobleaching of the CPN samples remained relatively low. A slightly stronger effect was observed for PTB7@F127 CPN samples (Figure S1.4d), while no change in the photobleaching behaviour was recorded for the PTB7@PSMA CPN samples (Figure S1.4c). These results seem to correlate with the different efficiencies of singlet oxygen production among the PTB7 CPN samples: the PTB7@F127 CPNs were the most efficient, exhibiting an approximately 7.5-fold improvement compared to bare PTB7 (see Figure 5.2(c)), while for PTB7@PSMA CPNs, the singlet oxygen production was completely quenched (Figure 4 of the main

text). This suggests that the singlet oxygen produced by the PTB7@F127 CPNs is somehow responsible for its increased photobleaching: at lower powers, the singlet oxygen production is negligible and PTB7@F127 CPNs behave in a similar way to the bare PTB7 and PTB7@PSMA CPNs; while at higher powers, the non-zero singlet oxygen production contributes to the temporal decrease of its fluorescence under continuous illumination. This property of PTB7@F127 CPNs could make it particularly suitable for biomedical applications as the outstanding resistance to photobleaching at lower power excitation laser can achieve long term imaging and at higher excitation powers, its photosensitization properties can be unlocked for photodynamic therapy.

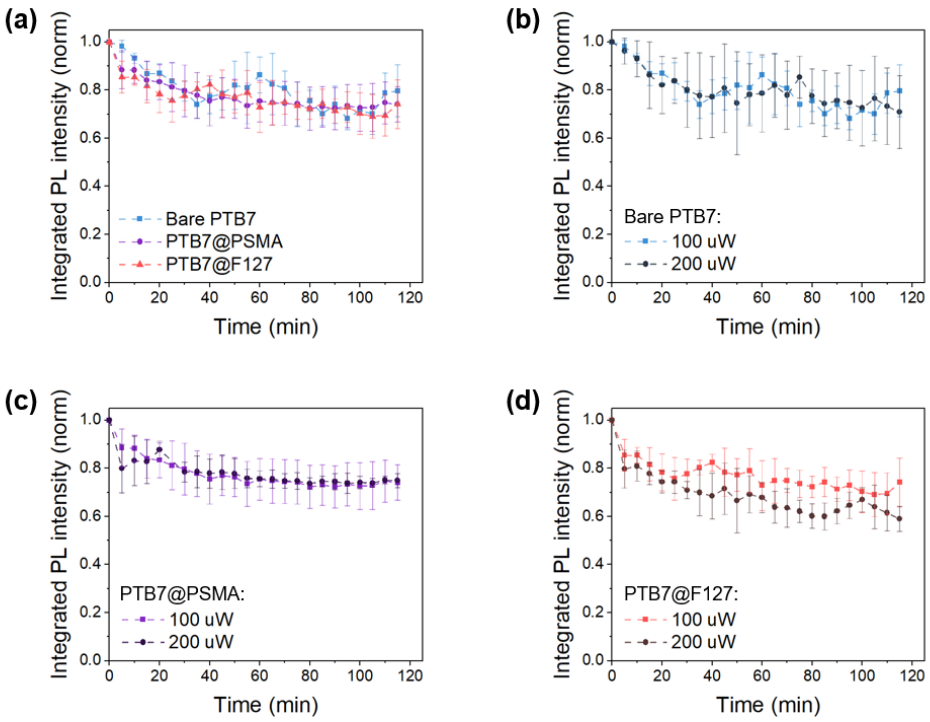


**Figure S1.4. Photobleaching resistance of PTB7 CPNs under prolonged stimulation.** Schematic illustration describing the slow fluorescence decrease of different type of **(a)** CPNs with 100 µW 635 nm laser stimulation for 2 hours and **(b)** bare PTB7 and **(c)** PTB7@PSMA CPNs and **(d)** PTB7@F127 CPNs are compared at 100 µW and 200 µW 635 nm laser stimulation for 2 hours.

It should be noted that the photobleaching of our PTB7@F127 CPNs was not permanent. Upon illumination at 200 μW for 25 mins, and subsequent removal of excitation, the fluorescence intensity of PTB7@F127 CPNs recovered to its original level (Figure S1.5). The reversible photobleaching suggests that no permanent changes occur to the PTB7 and F127 structures,[3] or their packing and that the cause of the photobleaching is transient in nature. In addition, the recovery time of ~2 hours allows for repeated treatment, if needed, since the half-time blood circulation for ~180 nm soft nanoparticles is expected to be on the order of 1 day.[4]

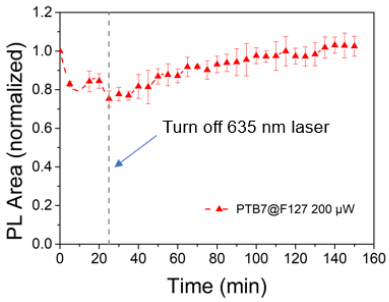


**Figure S1.5. Fluorescence recovery after photobleaching of PTB7@F127 CPNs.** The PTB7@F127 CPNs was photobleached for 25 mins using 200 μW of 635 nm laser. Fluorescence recovery was subsequently monitored by acquiring images every 5 mins (indicated by the dash line).

***Temporal stability of CPN samples***

The temporal stability of the synthesized PTB7 CPN samples was monitored for a period of 6 months and evaluated in the first instance by noting any changes in the size and optical properties of the CPNs. Figure S1.6 compares the hydrodynamic radii of the as-prepared CPN samples to the 6 month-old samples. The results show a significant change in the size of the bare PTB7 (approximately 50% reduction), but a reduced reduction in the size of the PTB7 CPNs coated with PSMA (~10%; statistically significant) and a minimal change in the hydrodynamic size of the PTB7@F127 CPNs

(~3% change *versus* 2% standard error). The reduction in the size of the bare PTB7 suggests some "unravelling" of the polymer chains and subsequent desorption from the surface, which is mitigated by the presence copolymer coatings.

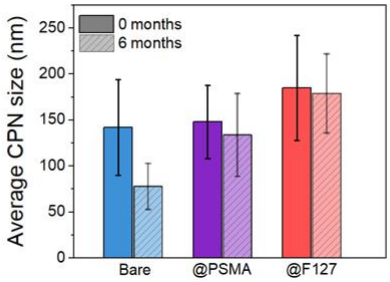


**Figure S1.6. Changes to the hydrodynamic size of the CPNs upon sample aging.** The average hydrodynamic size of the bare PTB7 (blue bars), PTB7@PSMA (purple bars) and PTB7@F127(red bars) CPNs are compared at different time points following their synthesis. The un-patterned darker filled bars correspond to the CPNs sizes immediately following the synthesis of the samples, while the lighter patterned bars correspond to the sizes of the CPNs following a 6 months storage in the dark at 4˚C. The error bars represent the standard deviation of particle sizes within each sample (and not the standard error in the average CPNs size for the sample).

Interestingly, very small changes were observed in the optical spectra of the three samples, especially in relation to the optical features corresponding to the excitation from the ground to the first excited state of the CPNs, *i.e.* the main absorption peaks with their 2-level vibronic structures and the emission peaks (Figure S1.7). This suggests that the overall structure of the PTB7 chains remains stable, with only a small level of reorganization over time. The organization of the chains necessarily results in the generation of different excitation species, resulting in slight shifts of the PL peaks, slight changes in the ratio of the absorbances of the two peaks (corresponding to transitions

into the different vibronic levels of the first excited state) and changes in the fluorescence QY of the samples. Regarding the latter, and despite minimal changes in other properties of the PTB7@F127 CPNs (Figure S1.9), fluorescence QY of this sample approximately halved over the 6-month monitoring period (0.6-0.8% for the 6-month-old sample, compared to 1.4% for the as-prepared sample, Figure S1.8). Hence, even minimal structural changes can lead to strong changes in the fluorescence properties of the CPNs particles.

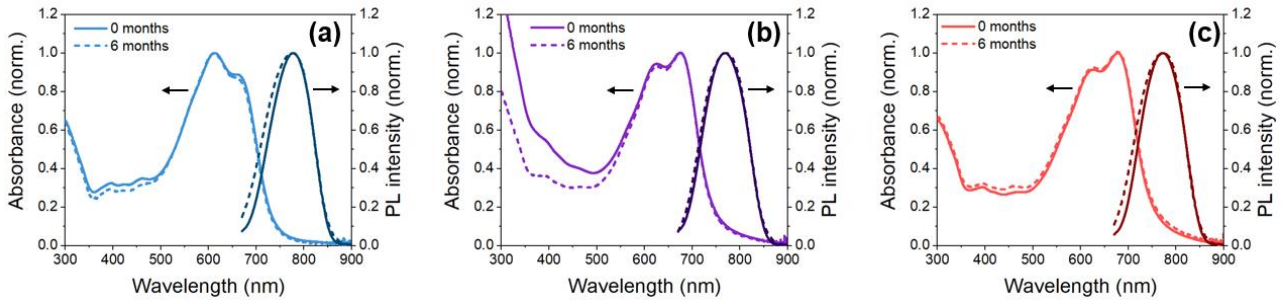


**Figure S1.7. Changes in absorbance and fluorescence spectra of PTB7 CPNs upon aging.** The absorbance (lighter colours) and fluorescence (darker colours) spectra of the **(a)** bare PTB7, **(b)** PTB7@PSMA CPNs and **(c)** PTB7@F127 CPNs are compared at 0 months (solid lines) and 6 months (dashed lines) after the synthesis of the sample.

Of interest is also the fact that the change in the optical properties and the fluorescence QY of the samples depended on how they were stored. The samples could either be stored as synthesized, and purified by centrifugation immediately prior to use ("a+c" = "aged + centrifuged"), or they can be purified by centrifugation immediately following synthesis and then stored ("c+a"). As can be seen from Figure S1.8, small but distinguishable changes in the optical properties of these samples were

observed, with either an increase or a decrease in the absorption at higher energies, and a varying degree of broadening of the emission peak (although in both cases it was small). In addition, the resulting fluorescence QY yields were also different for the two methods of storing the sample, with a slightly smaller reduction in the QY for the sample that was left unperturbed immediately after synthesis (0.76% for the "a+c" sample *versus* 0.58% for the "c+a" sample). It is unclear how the minute changes in the absorbance and emission peaks correlate with the large and differing reduction in the fluorescence QYs of these samples, and further investigation into the photophysics of the PTB7@F127 CPNs are required to elucidate the responsible mechanisms.

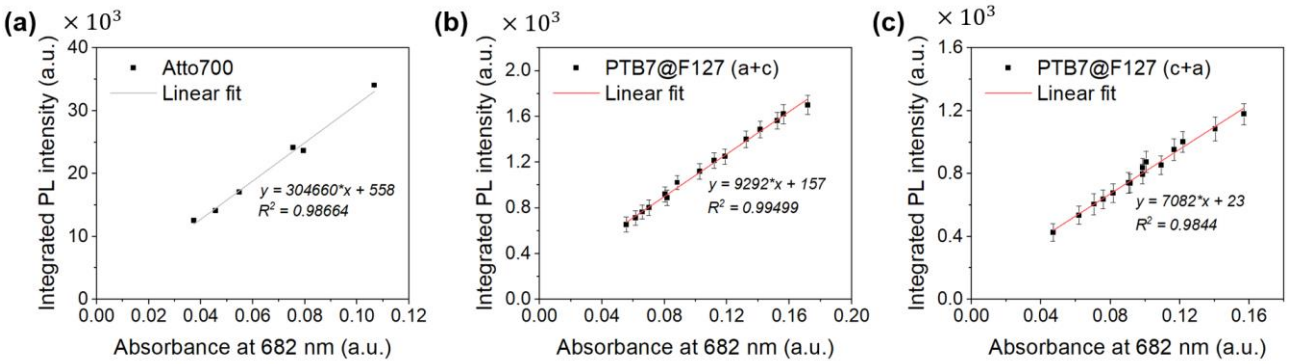


**Figure S1.8. Determination of fluorescence quantum yield of 6-month-old PTB7@F127 CPNs.** **(a)** Calibration of the absorbance by the sample at the excitation wavelength *vs* fluorescence signal measured from the fluorescence standard sample (Atto700; 25% QY). **(b)** and **(c)** show the dependence of fluorescence intensity *versus* absorbance at excitation wavelength for the PTB7@F127 sample, which was either **(b)** aged first and then purified by centrifugation (a+c), or **(c)** purified by centrifugation and then aged (c+a). The QYs of these two samples was then obtained by multiplying the QY of the standard (25%) and the corresponding ratio of the slopes obtained, yielding values of (0.76 ± 0.4)% and (0.58 ± 0.3)% for the (a+c) and (c+a) samples respectively. Full details of the method can be found in Section 4 below.

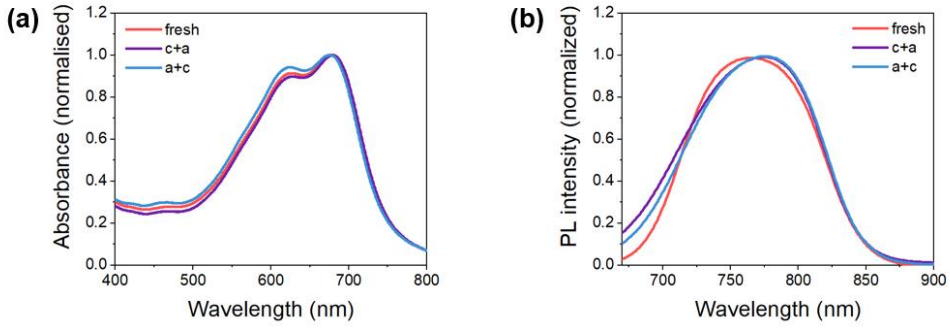


**Figure S1.9. Changes to absorbance and fluorescence spectra of PTB7@F127 CPNs with aging.** The **(a)** absorption and **(b)** fluorescence spectra of PTB7@F127 CPNs immediately after synthesis and purification *via* ultracentrifugation ("fresh"; red lines); 6 months after synthesis and purification *via* ultracentrifugation ("c+a", purple lines); and 6 months after synthesis, purified *via* ultracentrifugation immediately prior to measurement ("a+c", blue lines).

**Characterization of PTB7 CPN sizes**

The sizes (diameters) of the prepared CPN samples were characterized using three methods: dynamic light scattering (DLS), atomic force microscopy (AFM) and transmission electron microscopy (TEM).

The DLS method yielded the hydrodynamic diameters of the CPNs in aqueous solutions. Measurements were obtained using the Malvern Zerasizer NanoZS. For these measurements, samples were diluted to a final concentration of 5 µg/ml and 2 mL of this dilute CPN sample was then used in a dedicated disposable cuvette. Each DLS measurement consisted of 3 repeats of 10 runs, and the ZetaSizer software applied the model to output the size distribution data and averages directly from each measurement.

For AFM measurements, cover-slip substrates were first washed using Hellmanex III solution (Helma), according to manufacturer instructions, and then dried under $N_2$ flow. Onto this, 20 µL of

10 μg/ml CPNs solution was drop-casted and left to air-dry. Alternatively, 100 μL of this CPNs solution was spin-coated at 2000 rpm for 30 sec using Laurell WS-650HZB Spin Coater. The prepared CPNs-containing substrates were then imaged using the Bruker Icon Dimension Atomic Force Microscope.

For TEM measurements, 6 μL of 20 μg/ml CPNs solution was drop-casted onto a TEM grid (Fisher Scientific, 400 mesh carbon grids) and left to air-dry. Imaging was performed on a JEOL 1400 transmission electron microscope, operated at 120 kV.

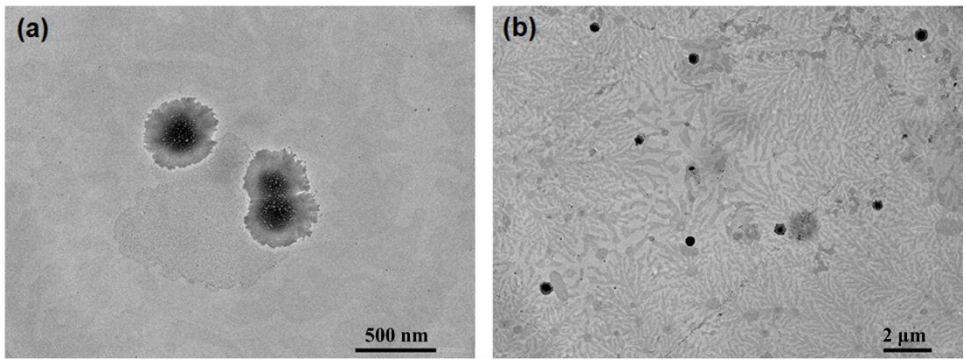


**Figure S2.1. TEM images of PTB7@F127 CPNs in water at high (a) and low (b) magnification.** **(a)** TEM image of PTB7@F127 CPNs at high magnification and **(b)** at low magnification. The fractal patterns that can be seen in (b) are formed by the excess F127 capping molecules present in the PTB7@F127 CPN solutions prior to purification by centrifugation.

***Dispersion stability of PTB7@PSMA CPN solutions***

The dispersion stability of PTB7@PSMA CPNs at different concentrations was evaluated using DLS measurements (Figure S2.2). Just like the PTB7@F127 CPN sample (described in the main text of the manuscript), the PTB7@PSMA CPNs shown an overall excellent dispersion stability over a wider range of concentrations, with a slightly increasing average size and polydispersity of the sample

at higher concentrations. However, the emerging contribution to DLS intensity at higher particle sizes for high sample concentrations, indicates that the PTB7@PSMA sample has a higher tendency to aggregate when compared to PTB6@F127 CPNs.

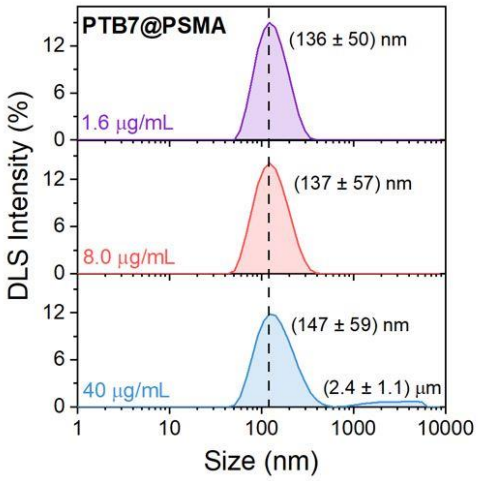


**Figure S2.2. Hydrodynamic sizes of PTB7@PSMA CPN solutions of various concentrations.** The concentrations of CPN samples are indicated in the bottom right corner of each panel, in colors corresponding to that of the plot data. The dashed line is included as a guideline only and represents the average size of the PTB7@PSMA CPNs for 1.6 μg/mL concentration. The numbers in brackets next to each peak indicate the average particle size for that peak and the corresponding standard deviation, as $(d_{av} \pm st.dev.)$.

***A note on the fluidity of the F127 shell***

We would like to note here that the F127 shell remains fluid even after removal of the loosely bound F127 strands from the surface of the CPNs by centrifugal ultrafiltration. This is clearly evidenced by the AFM and TEM images of the PTB7@F127 samples. Figure 1 of the main manuscript shows and AFM image of PTB7@F127 CPNs, in which the spread of F127 shell around each PTB7 core can be

easily distinguished. The spread of the fluid shell is caused by the evaporation and immersion forces experienced by the shell upon the drying of the sample. Preparation of samples for SEM/TEM imaging, which likewise involves the drying of the sample, caused similar effects although to a smaller degree, presumably because of different F127/substrate interactions. Nonetheless, the comparison of TEM images in Figure S2.1 shows a clear difference between the filtered and non-filtered samples: for filtered samples, particles have clearly distinct F127 shells, whereas the loosely-bound F127 in non-filtered samples separates from the CPN surface and forms a fractal pattern on the TEM grid.

**Comparison of DLS and AFM volumes of PTB7 CPNs**

The volumes of the PTB7@F127 CPNs were estimated both from the DLS and the AFM data. For the DLS data, it was assumed that the particles are spherical in shape when dispersed in aqueous solutions. Their volume can then be approximated by:

$$V_{DLS} = \frac{4}{3}\pi\left(\frac{d_{DLS}}{2}\right)^3$$

where $d_{DLS}$ is the average diameter obtained from dynamic light scattering measurements (ZeraSizer, Malvern), which was determined to be 185 nm with a standard deviation of 57 nm. Substituting these values into above equation yields a value of $3.3 \times 10^{-3}$ fL (with a standard deviation of $3.1 \times 10^{-3}$ fL).

The shapes of the particles in the AFM images were clearly not spherical, hence a simple approximation was not possible. To determine the mean volume of particles from the AFM data, the AFM images were first corrected for the background and any contributions from impurities deposited on the surface (Figure S3.1(a)). The counting and segregation procedure described by

http://pythonvision.org/basic-tutorial/ was then used to delineate and count the number of CPNs particles in the AFM image (Figure S3.1(b)), and finally segregate the scanned area into regions occupied by each particle (Figure S3.1(c)) using bespoke python3.2 code.

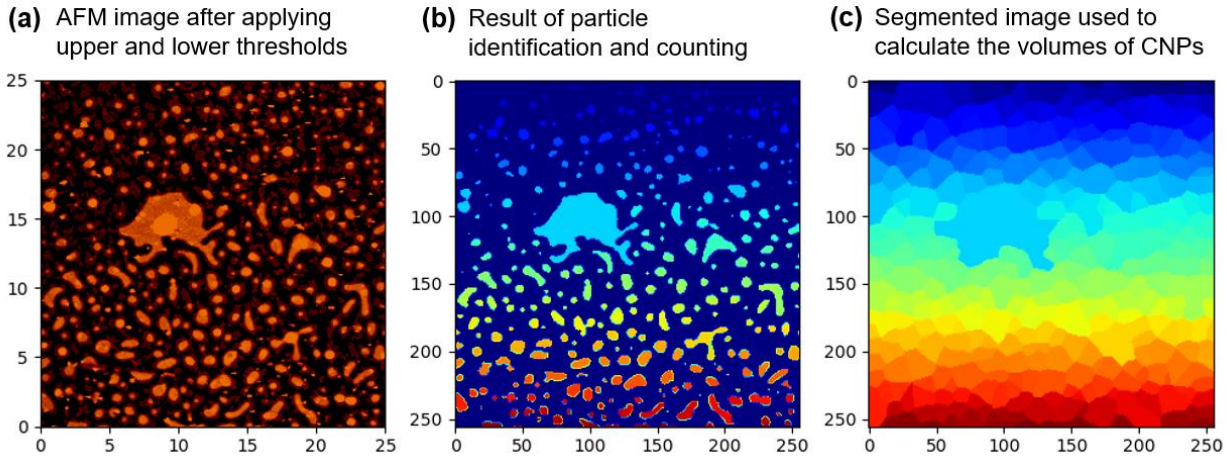


**Figure S3.1. Results of particle counting and area segmentation. (a)** The AFM image (25 x 25 μm$^2$) used to calculate $V_{AFM}$, after background correction and reduction of contributions from impurities deposited on the surface *via* an application of lower and upper thresholds. **(b)** Application of an intermediate threshold resulted in delineation of each particles' and identification of the total number of particles in the AFM image (328). The color in the image corresponds to the index of the particle on a jet colorscale, from 1 to 328. **(c)** Result from (b) was used to segment the area of the AFM image into smaller areas, corresponding to the regions occupied by each individual particle. The AFM height data from (a) was integrated over each of these areas to obtain the volume of each particle. The x and y scales of (b) and (c) are in pixels.

The height data at every pixel ($h_i$) in each of these regions was then integrated to yield an approximation for the volume of each particle, according to:

$$V_{particle} = \sum_{i=1}^{itot} h_i * \Delta x * \Delta y$$

here $\Delta x$ and $\Delta y$ were the x and y sizes of each pixel in nm, respectively. The results of these calculations are histogrammed in Figure S3.2. The mean and the standard deviation of the results were finally obtained using Microsoft Office Excel, yielding the average volume of $V_{AFM} = (4.7 \pm 0.2) \times 10^{-3}$ fL (with a standard deviation of $4.2 \times 10^{-3}$ fL).

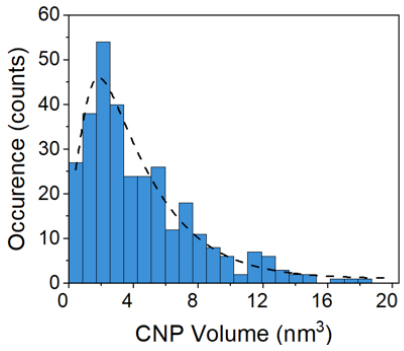


**Figure S3.2. Histogram of PTB7@F127 CNP volumes obtained from AFM data.** A total of 328 particles were identified by the delineation code, and the volume of each was calculated by summing the AFM height data over segmented areas of Figure S3.1(c).

The two volumes are of the same order of magnitude and are well within each other's standard deviations, but they do differ by ~23%. The discrepancy in the two values is most likely due to the deformation of the CPNs during the preparation of the AFM samples by spin-coating, and the much smaller sample size for the AFM data compared to the DLS measurements.

***Comparison of AFM images of F127 and PSMA-coated PTB7 CPNs***

Since the rigidity of the polymer can influence the sizes of the particles measured by DLS, it was important to confirm the relative sizes of the coated samples using other means. For this reason, we have imaged air-dried PTB7@F127 and PTB7@PSMA samples using Atomic Force Microscopy (Figure S3.3). The results confirmed that, on average, PTB7@PSMA CPNs are smaller than the F127 counterparts, with the majority of the difference coming from the size of the copolymer shell, *i.e.* the PTB7 core sizes were approximately the same for both samples.

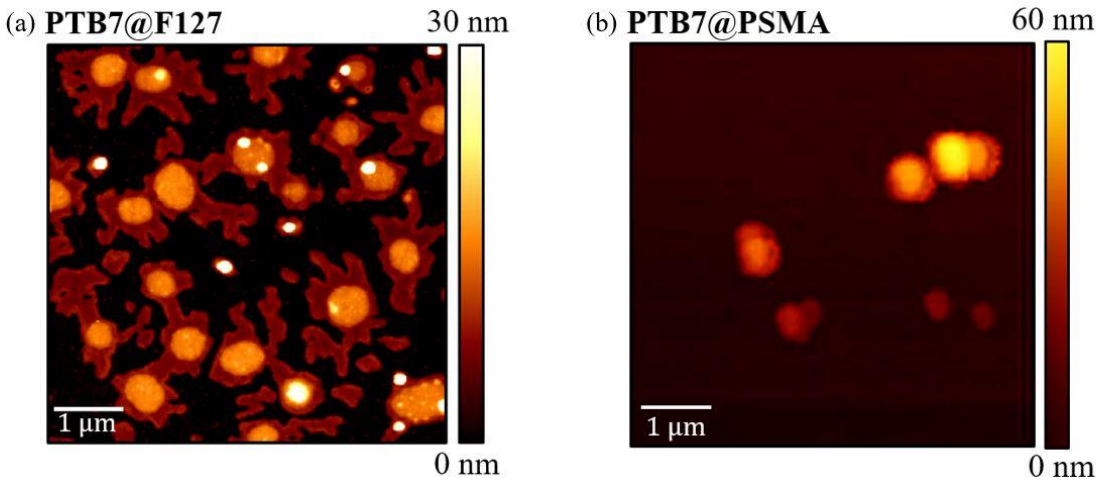


**Figure S3.3. AFM images of coated PTB7 CPNs.** AFM image of (a) PTB7@F127 CPNs and (b) PTB7@PSMA CPNs, air-dried on a microscope slide. The white line in each panel corresponds to 1 µm distance. The color bars show the corresponding AFM heights for the two scans.

**Optical characterization of CPN samples**

***UV-vis and steady-state fluorescence measurements***

The absorption spectra of ATTO700 and CPNs in water were measured at room temperature, in the 300-900nm spectral range using a UV-2600 spectrometer from Shimadzu. The emission spectra were

recorded in the 600-900 nm spectral range of using an Agilent Cary 60 spectrometer. For all measurements, 1 mL of test solution was placed inside the 1.4 mL fluorescence microcuvettes (Helma) of 1 cm path length.

***Fluorescence quantum yield measurements***

The fluorescence quantum yield (QY) of CPN samples was measured *via* the relative method, using an aqueous solution of the Atto700 dye as a reference ($QY_{\mathrm{ref}} = 0.25$). A concentration series of both the Atto700 and the PTB7@F127 CPNs were prepared by diluting the respective samples in DI water, to achieve samples with absorptions in the 0.1-0.2 and 0.1-0.35 ranges respectively for the two samples, at 682 nm. The fluorescence spectra of all samples were then recorded in the 700-900 nm spectral range, using 682 nm as the excitation wavelength, and keeping the excitation and emission slit widths constant at 5 nm. An estimated integrated fluorescence intensity ($I_{\mathrm{PL}}$) was obtained from the data by first smoothing the raw data (see red curve in Figure S4.1c) and then calculating the integrated area under the smoothed curve according to:

$$I_{\mathrm{PL}} = \sum_{i=1}^{N} I_i$$

where $i$ are the individual data points in the smoothed data and $N$ is the total number of the data points. During these calculations, the wavelength step ($\Delta\lambda = 1\,\mathrm{nm}$) and the spectral range of integration (700-900 nm) were same for all sets of data. The error in the integrated fluorescence intensity ($\Delta I_{\mathrm{PL}}$) was also estimated by calculating the total root-mean-square deviation between the raw and smoothed data (Figure S4.1c):

$$\Delta I_{\mathrm{PL}} = \sum_{i=1}^{N} \sqrt{\left(I_i^{raw} - I_i^{smoothed}\right)^2}$$

This procedure was repeated for every sample in the dilution series, and then plotted against absorption at the excitation wavelength (Figure S4.1a and S4.1b). Straight line plots of $I = K * A(682\ nm) + B$ form were fitted to the Atto700 and PTB7@F127 sets of data (Origin 2019b) and the slopes ($K$) were then used to calculate the QY of the PTB7@F127 sample, according to:

$$QY_{\mathrm{PTB7@F127}} = \frac{K_{\mathrm{PTB7@F127}}}{K_{\mathrm{atto700}}} * QY_{\mathrm{atto700}}$$

where $K_{\mathrm{PTB7@F127}}$ and $K_{\mathrm{atto700}}$ are the slope of the line fits for the PTB7@F127 CPNs and Atto700 solutions, respectively. The error in the QY of the PTB7@F127 sample was obtained using:

$$\Delta QY_{\mathrm{PTB7@F127}} = QY_{\mathrm{PTB7@F127}} * \sqrt{\left(\frac{\Delta K_{\mathrm{PTB7@F127}}}{K_{\mathrm{PTB7@F127}}}\right)^2 + \left(\frac{\Delta K_{\mathrm{atto700}}}{K_{\mathrm{atto700}}}\right)^2}$$

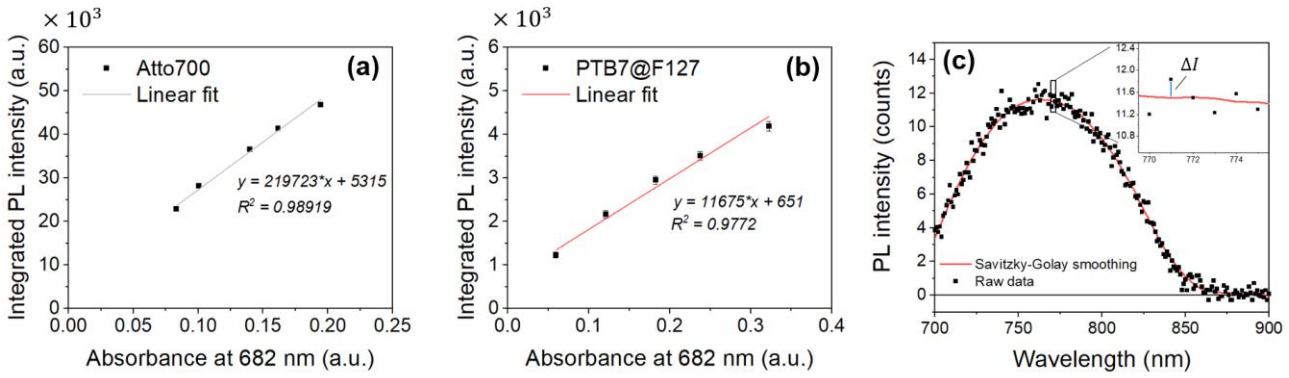


**Figure S4.1. Determination of fluorescence quantum yield of PTB7@F127 CPNs.** Figure shows integrated fluorescence intensities for **(a)** ATTO 700 and **(b)** PTB7@F127 CPNs of different concentrations, and therefore different absorbances at the excitation wavelength (682 nm). The grey and red lines are the corresponding linear fits to the data. Panel **(c)** illustrates the approach taken to calculate the error in the integrated fluorescence intensity of each sample. Each spectrum was first smoothed, and the absolute differences between the raw and smoothed data ($\Delta I_i$) were summed to obtain the total error in the estimate of $I_{PL}$.

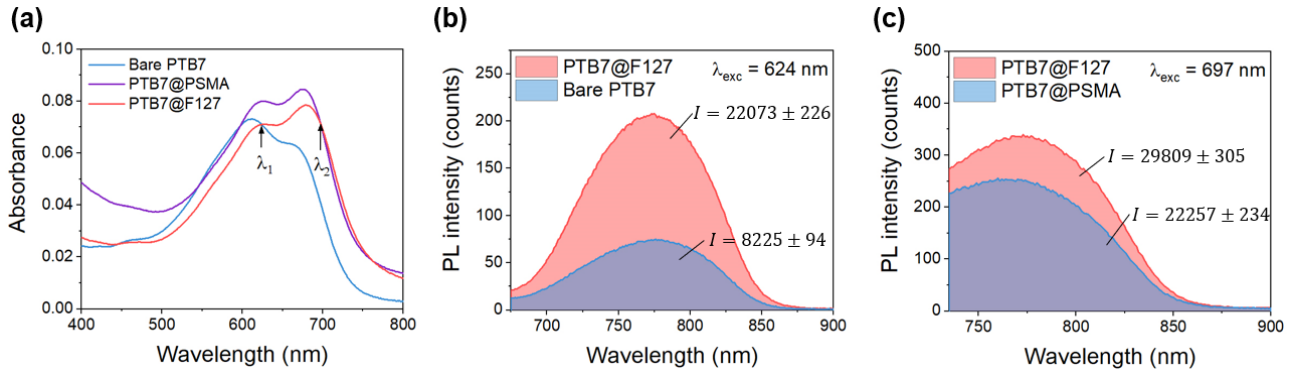


**Figure S4.2. Determination of the fluorescence quantum yield (QY) of bare PTB7 and PTB7@PSMA CPNs. (a)** The absorbance spectra of bare PTB7(blue), PTB7@PSMA CPNs (purple) and PTB7@F127 CPNs (pink) samples used for determination of fluorescence QYs of bare PTB7 and PTB7@PSMA CPNs. The excitation wavelengths to use in fluorescence measurements ($\lambda_1$ and $\lambda_2$) were chosen such that each sample of unknown wavelength had same absorbance as PTB7@F127 CPNs. **(b)** and **(c)** compare the fluorescence intensities of the PTB7@F127 CPNs with those of (b) bare PTB7 and (c) PTB7@PSMA sample. Also shown are the fluorescence intensities of each sample, integrated over the shown spectral range ($I$).

Using above method and a value of 25% for $QY_{\text{atto700}}$, the QY of PTB7@F127 CPNs was determined to be ~$(1.33 \pm 0.32)$% which is within our expectation, with literature values of ~2% for thin PTB7 films.

The QYs of bare PTB7 and PTB7@PSMA samples were then obtained using a simplified relative method, with the PTB7@F127 sample acting as a reference. For these measurements, all samples were first diluted to have absorptions of less than 0.1 at the peak, and the excitation wavelengths were chosen such that the absorptions were the same for a single pair of samples, as illustrated in Figure S4.2a. The samples were then analyzed in pairwise fashion, using the same set of settings to record the fluorescence spectra of samples in each pair. For bare PTB7, the test and the reference

(PTB7@F127) samples were both excited at 624 nm, and the fluorescence spectra were recorded in the 670 – 900 nm spectral range (Figure S4.2b). For PTB7@PSMA CPNs, the test and the reference samples were excited at 697 nm and as a result their fluorescence spectra were recorded over a narrower range of 735 – 900 nm (Figure S4.3c). The integrated fluorescence intensities of these all samples were then calculated using the procedure described above (results shown in respective panels of Figure S4.2), and the fluorescence QY of the bare and PSMA-coated PTB7 CPNs were then calculated according to:

$$QY_{\text{sample}} = \frac{I_{\text{sample}}}{I_{\text{F127}}} * QY_{\text{F127}}$$

$$\Delta QY_{\text{sample}} = QY_{\text{sample}} \sqrt{\left(\frac{\Delta QY_{\text{F127}}}{QY_{\text{F127}}}\right)^2 + \left(\frac{\Delta I_{\text{sample}}}{I_{\text{sample}}}\right)^2 + \left(\frac{\Delta I_{\text{F127}}}{I_{\text{F127}}}\right)^2}$$

where $I$'s are the integrated fluorescence intensities of the samples, and the subscripts "sample" and $\text{F127}$ refer respectively to CPN samples of unknown fluorescence QY and the PTB7@F127 sample. The fluorescence QYs of $(0.5 \pm 0.1)\%$ and $(1.0 \pm 0.2)\%$ were obtained for the bare PTB7 and PTB7@PSMA CPNs respectively.

***A note on red-to-NIR absorption and CPN concentration***

In several figures presented in the main text of the manuscript and in this supplementary file, the fluorescence spectra of CPN samples were measured at an excitation wavelength where the absorbances of the three CPN samples were equal, with the excitation wavelength selected within the main absorbing region falling between 500 and 800 nm. In this spectral region, neither the F127 nor the PSMA absorb and hence PTB7 is the main contributor to any extinction observed (Figure S4.3). Thus, a similarity of extinction in the red-NIR spectral region by different PTB7 CPNs, combined with their comparable sizes, implies a similarity of sample concentrations.

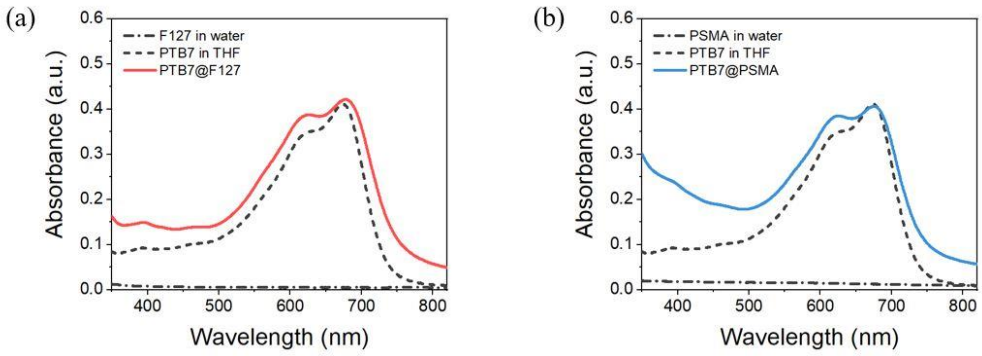


**Figure S4.3. Extinction of F127 and PSMA copolymers in water.** Figure compares the absorbances of (a) F127 and (b) PSMA copolymers in water to those of the correspondingly coated PTB7 CPNs. In both cases, the copolymer contributes negligibly to absorption of respective CPN samples in the 500-800 nm region.

***Normalized optical spectra of all samples***

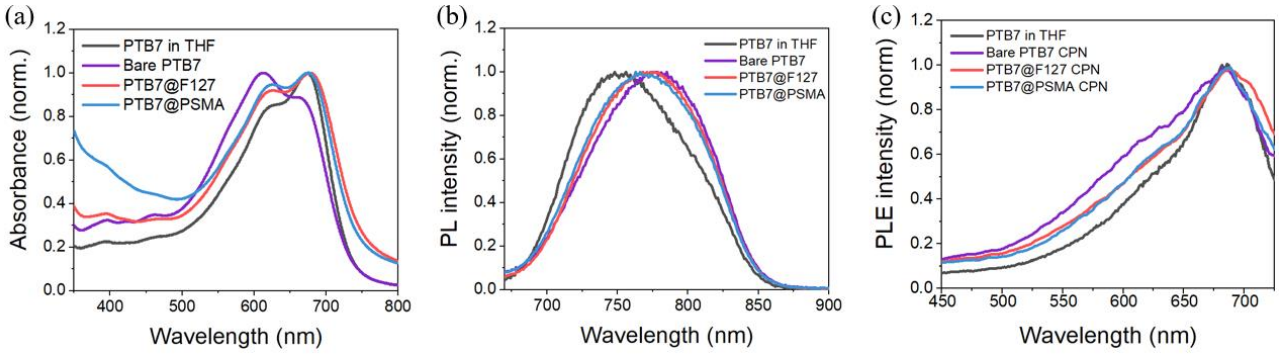


**Figure S4.4. Normalised optical spectra of all CPN samples and that of a PTB7 solution.** Panels (a), (b) and (c) compare, respectively, the normalized steady-state absorption, photoluminescence and photoluminescence excitation spectra of PTB7 polymer dissolved in THF (black lines), bare PTB7 CPNs (purple lines), PTB7@F127 CPNs (red lines) and PTB7@PSMA CPNs (blue lines). In panel (c), the emission wavelength for the PLE measurements was set to the peak photoluminescence wavelength for each corresponding sample.

***Photoluminescence excitation spectra of all samples***

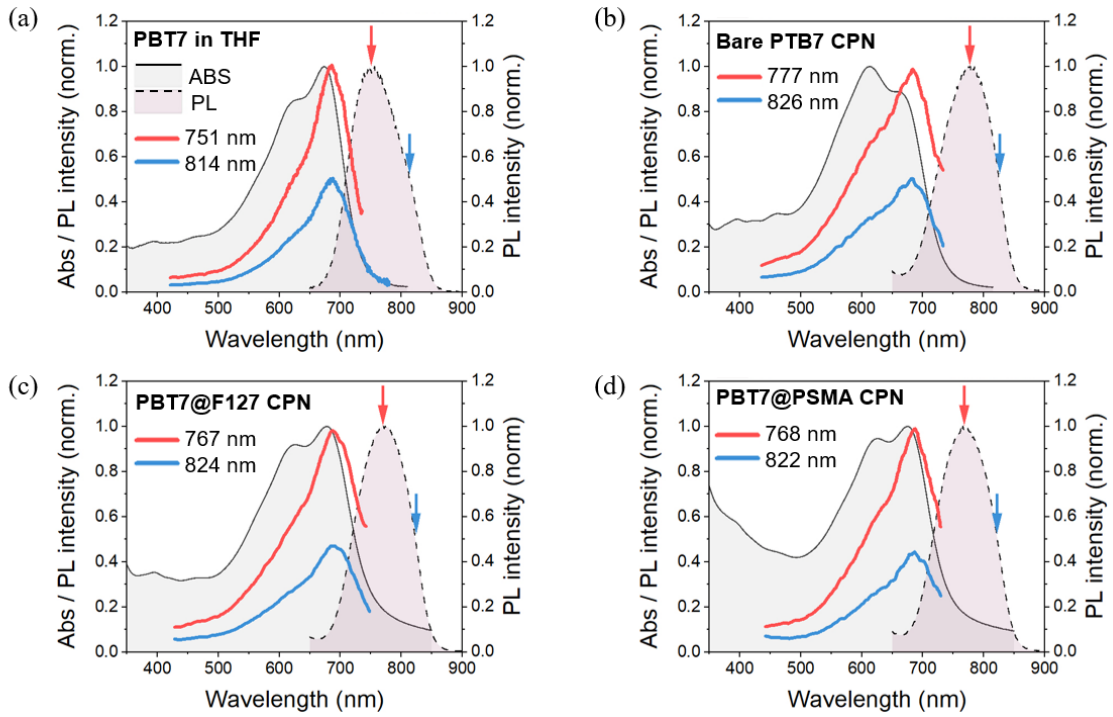


**Figure S4.5. Absorbance, photoluminescence and photoluminescence excitation spectra of all samples.** Panels (a), (b), (c) and (d) compare the absorbance (solid black line with gray shading), photoluminescence (dashed black line with pale grey/pink shading) and two photoluminescence excitation spectra (red and blue solid lines) for PTB7 solution in THF, bare PTB7 CPNs, PTB7@F127 CPNs and PTB7@PSMA CPNs, respectively. The colored arrows in each panel indicate the emission wavelength used to collect the respectively colored PLE spectrum. The emission wavelengths used are also indicated in the legend of each panel. For clarity, absorbance and photoluminescence spectra were normalized to 1 at peak wavelength. The PLE spectra were normalized to the values of normalized photoluminescence at the emission wavelengths used.

***Deconvolution of optical spectra into components***

Each of the normalized absorbance spectra in Figure S4.5(a) above was deconvolved into five Gaussian contributions (in energy scale) using the Multi Peak Fit analysis option of the Origin (2019b) software. The decision to use 5 components for the deconvolution of each spectrum was based on previous reports of similar procedures for PTB7 thin films and solutions,[5] but also on our inability to fit the curves successfully with a 4-Gaussian components model. The initial values for the positions of the peaks were approximated from the same reference. For each deconvolution, a fit with an R-square value of >0.999 was considered to produce a suitable quality of deconvolution. The results of the fitting procedure are shown in figure S4.6 below, and the extracted parameters of peaks 1 and 2 are summarized in Table S4.1. The errors quoted in the table are the direct results of the fitting procedure and are stated as outputted by Origin (2019b) software.

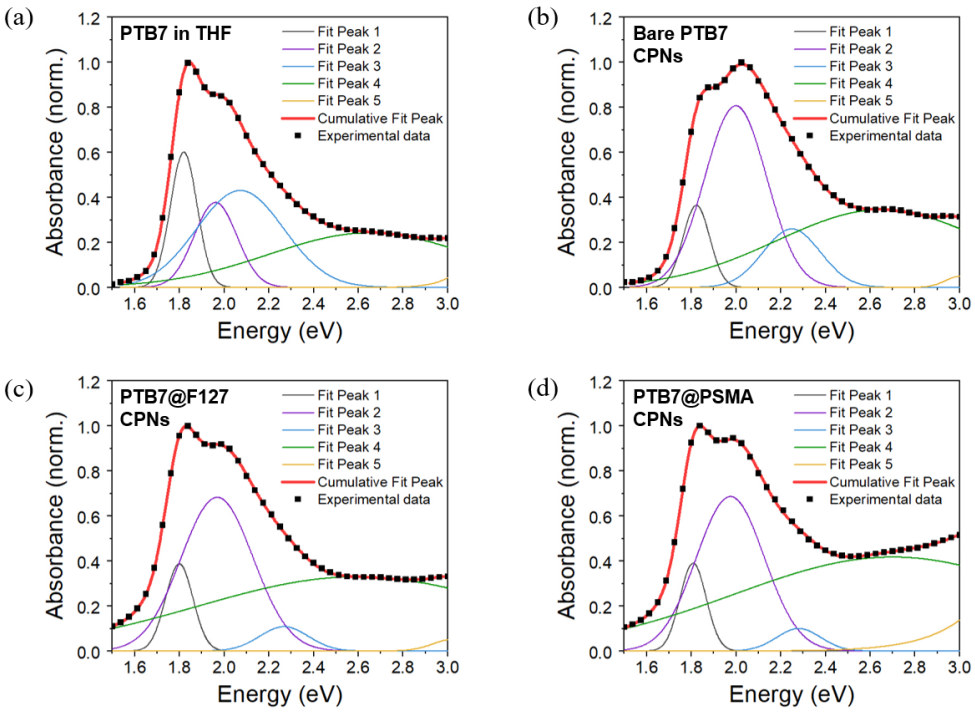


**Figure S4.6. Deconvolution of absorbance spectra into Gaussian contributions.** Panels (a)-(c) show, respectively, the results of the fitting procedure for PTB7 polymer dissolved in solution, bare

PTB7 CPNs, PTB7@F127 CPNs and PTB7@PSMA CPNs. For each case, the experimental data are shown as black scatter points, the Gaussian individual contributions are shown in solid colored lines and the sum of the contributions is shown in a thicker red solid line. The R-squared value for each fit was greater than 0.999.

A similar procedure was also applied to the normalized photoluminescence spectra of PTB7 polymer dissolved in THF and PTB7 CPNs dispersed in aqueous solutions. The results of these deconvolutions are shown in Figure S4.7 and Table S4.2.

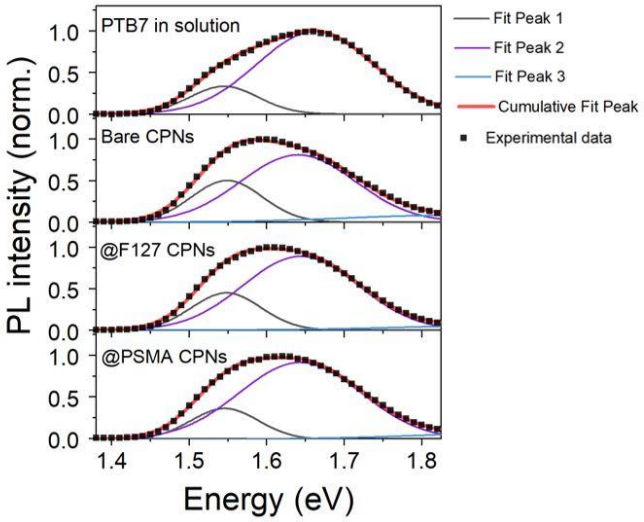


**Figure S4.7. Deconvolution of photoluminescence spectra into Gaussian contributions.** The results of the fitting procedure are shown (top-to-bottom) for PTB7 polymer dissolved in solution, bare PTB7 CPNs, PTB7@F127 CPNs and PTB7@PSMA CPNs. For each case, the experimental data are shown as black scatter points, the Gaussian individual contributions are shown in solid colored lines and the sum of the contributions is shown in a thicker red solid line. The R-squared value for each fit was greater than 0.99.

**Table S4.1. Summary of results obtained from deconvolution of absorption spectra into contributions from different excitation processes.**

| Sample | $E_{0-0}$ (eV) | $w_{0-0}$ (eV) | $E_{0-1}$ (eV) | $w_{0-1}$ (eV) | $A_{0-0}$ $/A_{0-1}$ | $R^2$ |
|---|---|---|---|---|---|---|
| PTB7 in THF | 1.8200 ± 0.0001 | 0.1199 ± 0.0002 | 1.9618 ± 0.0006 | 0.193 ± 0.001 | 0.99 ± 0.02 | 0.99996 |
| Bare PTB7 | 1.8231 ± 0.0002 | 0.1207 ± 0.0006 | 1.999 ± 0.001 | 0.277 ± 0.002 | 0.197 ± 0.005 | 0.99999 |
| PTB7@F127 | 1.7998 ± 0.0001 | 0.1232 ± 0.003 | 1.9691 ± 0.0007 | 0.3231 ± 0.0008 | 0.216 ± 0.002 | 0.99910 |
| PTB7@PSMA | 1.8080 ± 0.0001 | 0.1178 ± 0.0004 | 1.9752 ± 0.0004 | 0.3047 ± 0.0006 | 0.220 ± 0.002 | 0.99983 |

$E_{0-i}$ denote the peak energy of absorption contribution corresponding to an excitation from the ground state into the i$^{th}$ vibrational level of the excited state

$w_{0-i}$ denote the width of the absorption peak, at half maximum, corresponding to an excitation from the ground state into the i$^{th}$ vibrational level of the excited state

$A_{0-0}/A_{0-1}$ is the ratio of amplitudes of absorption peaks corresponding, respectively, to excitations from ground state into the 0$^{th}$ and 1$^{st}$ vibrational levels of the excited states

$R^2$ is the R-squared value for the multi-gaussian fit used to generate the data in the table

**Table S4.2. Summary of results obtained from deconvolution of photoluminescence spectra into contributions from different de-excitation processes.**

| Sample | $PL_{0-1}$ (eV) | $w_{0-1}$ (eV) | $PL_{0-0}$ (eV) | $w_{0-0}$ (eV) | $R^2$ |
|---|---|---|---|---|---|
| PTB7 in THF | 1.545 ± 0.001 | 0.089 ± 0.002 | 1.663 ± 0.001 | 0.150 ± 0.001 | 0.99870 |
| Bare PTB7 | 1.549 ± 0.002 | 0.092 ± 0.006 | 1.641 ± 0.007 | 0.15 ± 0.02 | 0.99827 |
| PTB7@F127 | 1.548 ± 0.002 | 0.090 ± 0.004 | 1.644 ± 0.003 | 0.15 ± 0.01 | 0.99883 |
| PTB7@PSMA | 1.547 ± 0.001 | 0.089 ± 0.003 | 1.646 ± 0.003 | 0.15 ± 0.01 | 0.99890 |

$PL_{0-i}$ denote the energy at peak of photoluminescence contribution corresponding to a de-excitation from the lowest excited state into the i$^{th}$ vibrational level of the ground state

$w_{0-i}$ denote the width of the photoluminescence peak, at half maximum, corresponding to a de-excitation from the lowest excited state into the i$^{th}$ vibrational level of the ground state

$R^2$ is the R-squared value for the multi-gaussian fit used to generate the data in the table

**Singlet oxygen production by PTB7@F127 CPNs.**

***General description of the method***

The production of $^1O_2$ by the fabricated CPNs was measured using SOSG as a chemical sensor. SOSG is a non-fluorescent molecule that is converted into a fluorescent form, SOSG-EP, upon reaction with $^1O_2$. In our case, production of $^1O_2$ was continuously stimulated using a red laser ($\lambda_{\text{stim}} = 635$ nm), which was absorbed by the PTB7 CPNs but not the SOSG. With this stimulation uninterrupted, the amount of SOSG-EP in the solutions was tested every 30 seconds by recording the SOSG-EP fluorescence spectrum ($\lambda_{\text{exc}} = 500$ nm), over a period of 3 seconds (Figure S5.1). By continuing the stimulation of $^1O_2$ production and collection of SOSG-EP fluorescence, the amount of $^1O_2$ produced by our CPNs could be monitored over time.

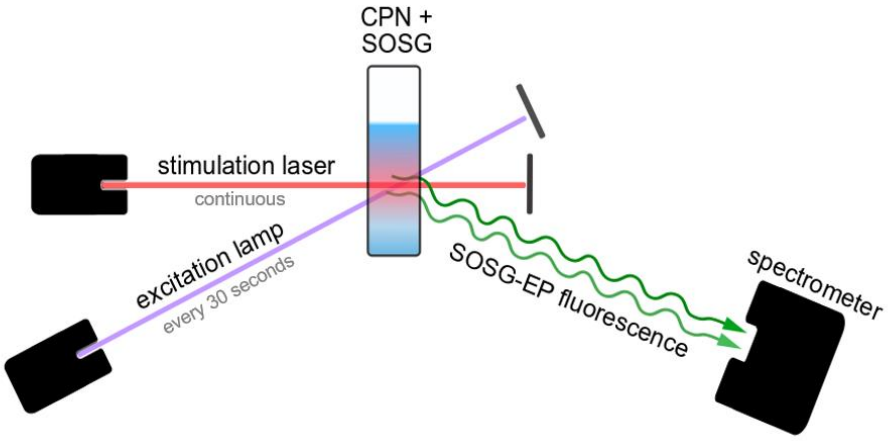


**Figure S5.1. Set-up used for measurements of ROS production by the PTB7 CPNs.** The CPN samples and SOSG were placed in a fluorescence cuvette. The production of $^1O_2$ was continuously stimulated by a red laser (635 nm, 4.5 mW, with an elliptical beam profile). The produced $^1O_2$ converted the non-fluorescent SOSG into its fluorescent form of SOSG-EP. The fluorescence from SOSG-EP was recorded every 30 seconds using a standard steady-state spectrometer ($\lambda_{\text{exc}} = 500$ nm).

The positive control involved the use of methylene blue (MB) instead of the CPNs in the test solution. The negative control was a sample to which no singlet oxygen producer was added (*i.e.* SOSG only in solution).

***Singlet oxygen production by PTB7@F127 CPNs and MB under prolonged stimulation***

In addition to experiments described in the main text of the paper, the production of $^1O_2$ by PTB7@F127 CPNs sample was also analyzed under prolonged stimulation conditions. The protocol for these experiments was identical to that found in the Methods section (and the same as the summary above), with the exception that the $^1O_2$ production was measured over a much longer stimulation period of 3 hours. For reference, the experiment was also repeated for our positive reference (MB dye). Figure S5.2(a) shows the results of these measurements, normalized to SOSG-EP fluorescence at the start of the measurements ($t = 0$). As can be seen from this graph, the ROS production by the PTB7@F127 CPNs increased continuously throughout the 3-hour measurement period. For MB, however, the SOSG-EP fluorescence decreased steadily after an initial 0.5 hour of increase, indicating a reduction in the rate of ROS production by this standard photosensitizer.

There exist several possibilities that may be responsible for the observed decrease of SOSG-EP signal. The first is that SOSG-EP reverts back to the non-fluorescent form (SOSG) or, even more likely, diffuses out of the excitation volume faster than the MB is producing singlet oxygen to drive the SOSG-to-SOSG-EP reaction. We tested whether this was a contributing factor by building up a substantial level of SOSG-EP signal and then turning off the stimulation laser, thereby prohibiting any further $^1O_2$ production by the photosensitizer.

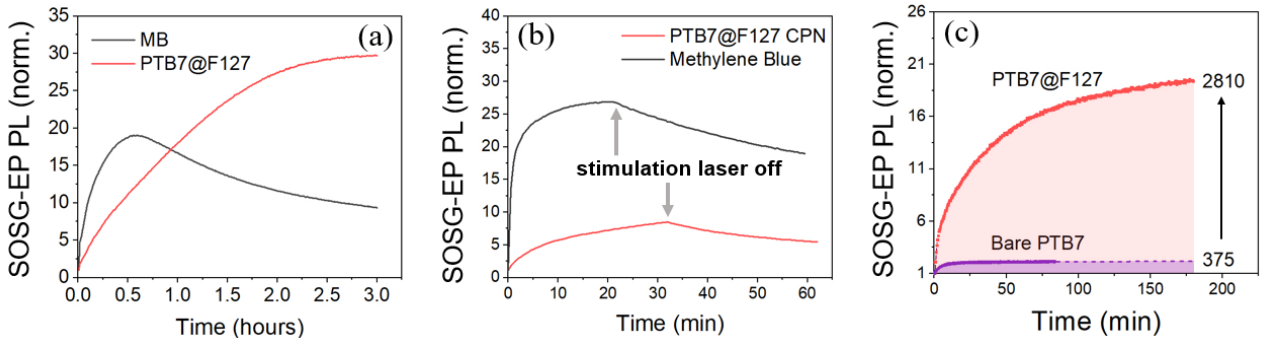


**Figure S5.2. Singlet oxygen generation by PTB7@F127 CPNs under prolonged stimulation.** Panel **(a)** shows the comparison of singlet oxygen production by the PTB7@F127 CPNs with the reference photosensitiser (methylene blue, MB) for a long stimulation period. In Panel **(b)**, the stimulation laser (635 nm) was turned off mid-way through the experiment, at times indicated by arrows in the graph. In the absence of stimulation, the fluorescence signal of SOSG decayed slowly over time. Panel **(c)** shows the evolution of the SOSG-EP PL signal for the bare PTB7 (purple) and PTB7@F127 (pink) samples of equal absorptions at the stimulation wavelength (635 nm). The numbers next to the data sets indicate the values of the SOSG-EP PL intensities for the two samples, integrated over a 3-hour period (shaded regions) with the bare PTB7 data extrapolated from 90 to 180 min. In the time period shown, the PTB7@F127 is estimated to have ~7.5-fold higher singlet oxygen generation efficiency compared to bare PTB7 sample.

As can be seen in Figure S5.2(b), the trends observed for Methylene Blue and PTB7@F127 CPNs were in this case similar, with a gradual decrease of SOSG-EP fluorescence over time, once the stimulation was removed. By fitting the SOSG-PL data post-stimulation with a mono-exponential function, the time constant for the SOSG-EP fluorescence decay was determined to be 18.3 ± 0.6 min. In the presence of stimulation (Figure S5.2a), the SOSG-EP fluorescence observed in the presence of MB was much slower, with an approximate time constant of 85.5 ± 1.1 min. However, in this case,

the production of $^1O_2$ was not inhibited, and therefore the continuous stimulation $^1O_2$ production by MB should have been much faster than the SOSG-EP fluorescence decay, and this was indeed the case at the beginning of the measurement (the first 30 minutes for MB) and for $^1O_2$ production by the PTB7@F127 CPNs, for which no decrease was observed at any point during the 3-hour measurement period.

A much more likely explanation is then that the observed decrease of SOSG-EP fluorescence after the 30 minutes is the result of reduced production of the $^1O_2$ by the MB after a prolonged excitation. The most likely cause is the degradation of the MB molecule through photobleaching and/or chemical destruction of the MB by the $^1O_2$ it itself produces.[6] In this regard, the performance of PTB7@F127 CPNs is notable since it seems to be stable against any such attacks. Continuous singlet oxygen production under prolonged excitation is critical for practical applications of the photosensitizers for PDT, and singlet oxygen-producing PTB7 CPNs developed in this work satisfy this requirement. This includes the bare PTB7 sample that was shown to have a continuously increasing generation of singlet oxygen over a 90-minute period, although at ~7.5-times smaller efficiency compared to the PTB7@F127 sample (see Figure S5.2c).

***Measurements of singlet oxygen QY for PTB7 CPN samples***

The QY for $^1O_2$ generation by CPNs was determined using a comparative method employing SOSG as the chemical fluorescence sensor for $^1O_2$. The process of converting SOSG to its fluorescence form SOSG-EP essentially constitutes a two-step reaction involving the singlet-oxygen producing sample (S) and the SOSG sensor molecule, with the first step requiring stimulation at frequency $\nu_1$ (red laser in our case):

1) $h\nu_1 + \mathrm{S} \rightarrow {}^1\mathrm{O}_2$

2) ${}^1\mathrm{O}_2 + \mathrm{SOSG} \rightarrow \mathrm{SOSG\text{-}EP}$

The two reactions occur with respective efficiencies of $\eta_{\mathrm{SO}}$ for the singlet oxygen production by the sample and $\eta_{\mathrm{EP}}$ for the SOSG to SOSG-EP conversion, with $\eta_{\mathrm{SO}}$ being the limiting factor during the measurement since SOSG is present in excess. The fluorescence signal obtained from SOSG-EP is therefore dependent on both the absorbance $A$ of the sample (at the stimulation wavelength) and its singlet oxygen yield $\eta_{\mathrm{SO}}$. It can be shown that at low sample concentrations, the fluorescence signal is linearly proportional to both, namely that:

$$I_{\mathrm{PL}} = K\eta_{\mathrm{SO}}A$$

where $K$ is a proportionality constant that incorporates all relevant experimental parameters that remain constant throughout the measurement, including the power of the stimulation lasers, the total time of the stimulation, the power of the excitation lamp, attenuation of fluorescence intensity by slits, efficiency of detector, extinction coefficient of SOSG *etc*. Therefore, a linear fit to $I_{\mathrm{PL}}$ *vs* $A$ data will yield a slope that is proportional to the quantum yield of the singlet oxygen production by the sample.

Figure S5.3(b) shows the $I_{\mathrm{PL}}$ *vs* $A$ data collected for MB in ethanol solution, in which it is known to have a singlet oxygen quantum yield of 52%. The SOSG fluorescence data were recorded after 5 minutes of continuous excitation with the 635 nm laser, as described earlier (Figure S5.3a). Using the value of the slope obtained from the linear fit to the $I_{\mathrm{PL}}$ *vs* $A$ data (= 6993.3 ± 835.5) and $\eta_{\mathrm{SO}}$= 0.52 yields a value of 13448.7 for our experimental constant $K$. Using this value for $K$, the singlet oxygen QY of other samples can now be measured, as long as the experimental conditions are kept the same. The red data points in Figure S5.3(b) show the results of the measurements for PTB7@F127

CPNs. The linear fit to the data yielded slope of 1136.1 ± 181.3, which implies that the singlet oxygen quantum yield of this sample in ethanol is 100%* 1136.1 / 13448.7 = (8.5 ± 1.7)%.

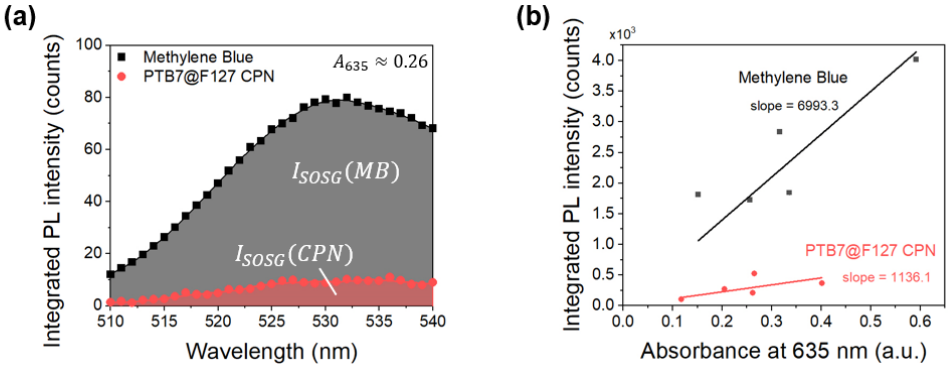


**Figure S5.3. The singlet oxygen generation quantum yield (QY) of PTB7 @F127 in ethanol.** (a) Fluorescence spectra of SOSG in the presence of Methylene Blue (black squares) and PTB7@F127 CPNs (red circles), for samples in ethanol with approximate absorbances of 0.26 at the stimulation wavelength of 635 nm. The integrated fluorescence intensity of SOSG was obtained by integrating the SOSG fluorescence over the shown spectral region (shaded areas). This was performed for solutions of different concentrations, yielding a plot of integrated SOSG fluorescence *versus* sample absorbance at 635 nm shown in panel (b). These data were fitted with linear fits; the slopes of these fits are indicated in (b) below sample names, and they were used to calculate the singlet oxygen QY of the PTB7@F127 CPNs.

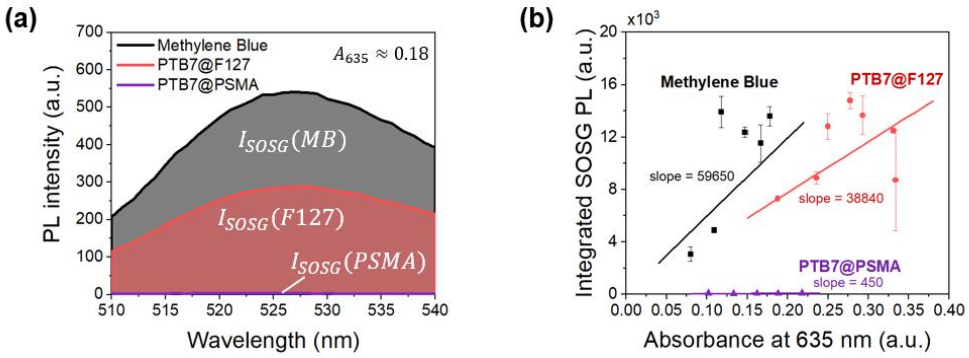


**Figure S5.4. The singlet oxygen generation quantum yield (QY) of PTB7 @F127 and PTB7@PSMA in water.** (a) Fluorescence spectra of SOSG in the presence of Methylene Blue (black line), PTB7@F127 CPNs (red line) and PTB7@PSMA CPNs (violet line), for samples in water with approximate absorbances of 0.18 at the stimulation wavelength of 635 nm. The integrated fluorescence intensity of SOSG was obtained by integrating the SOSG fluorescence over the shown spectral region (shaded areas). This was performed for solutions of different concentrations, yielding a plot of integrated SOSG fluorescence *versus* sample absorbance at 635 nm shown in panel (b). These data were fitted with linear fits; the slopes of these fits are indicated in (b) below sample names, and they were used to calculate the singlet oxygen QY of the PTB7@F127 CPNs and PTB7@PSMA CPNs.

The QY for $^1O_2$ generation by CPNs in water was determined using the same procedure, Figure S5.4(b) shows the $I_{PL}$ *vs A* data collected for MB in water, in which it is known to have a singlet oxygen quantum yield of 52%. The SOSG fluorescence data were recorded after 5 minutes of continuous excitation with the 635 nm laser, as described earlier (Figure S5.4a). Using the value of the slope obtained from the linear fit to the $I_{PL}$ *vs A* data (= 59650) and $\eta_{SO} = 0.52$ yields a value of 114711.5 for our experimental constant K. The red data points in Figure S5.4(b) show the results of

the measurements for PTB7@F127 CPNs and the violet data points show the results of PTB7@PSMA CPNs. The linear fit to the PTB7@F127 CPNs data yielded slope of 38840 ± 5500, which implies that the singlet oxygen quantum yield of this sample in water is 100%* 38840 ± 5500 / 114711.5 = (32.4 ± 4.8)%, while the PTB7@PSMA CPNs produced negligible amount of SO, with a QY of 0.38 ± 0.07%.

***Photochemical stability of CPNs during Singlet Oxygen measurements***

The polymeric backbones of conjugated polymers are highly susceptible to degradation in radical environments, often leading to poor photochemical stabilities of these polymers in the presence of highly reactive species such as singlet oxygen. To validate our results of singlet oxygen production measurements, it was important to exclude the possibility of any sample degradation during the measurements. To confirm this, the absorption spectra of the CPN/SOSG mixtures were recorded post- singlet oxygen production measurements. As can be seen in Figure S5.5(a) for bare PTB7 CPNs, the absorption spectra of these mixtures had clear signatures from both the PTB7 CPNs and the chemical sensor SOSG, allowing us to estimate contributions from both using a simple linear regression analysis.

Regression analysis was performed on the mixture absorption spectra, using pure CPN and SOSG spectra as basis for the linear regression ($A_{CPN}(\lambda)$ and $A_{SOSG}(\lambda)$ respectively). Regression analysis fitted the absorption spectra of the mixture to a linear combination of the two specified basis and a wavelength-independent background ($A_{bgr}$):

$$A_{CPN+SOSG}(\lambda) = A_{bgr} + k_{CPN} * A_{CPN}(\lambda) + k_{SOSG}A_{SOSG}(\lambda)$$

where $A_{bgr}$ and contribution coefficients $k_i$ were determined by the regression analysis. Figure 5.5(a) shows the result of the regression analysis ($A_{CPN+SOSG}(\lambda)$, dashed red line), as well as the calculated contributions from the CPNs and the SOSG ($k_i A_i$, purple and blue solid lines). In all cases, the result of the regression closely matched the as-measured absorption spectra of the CPN/SOSG mixture (R-squared values >0.999).

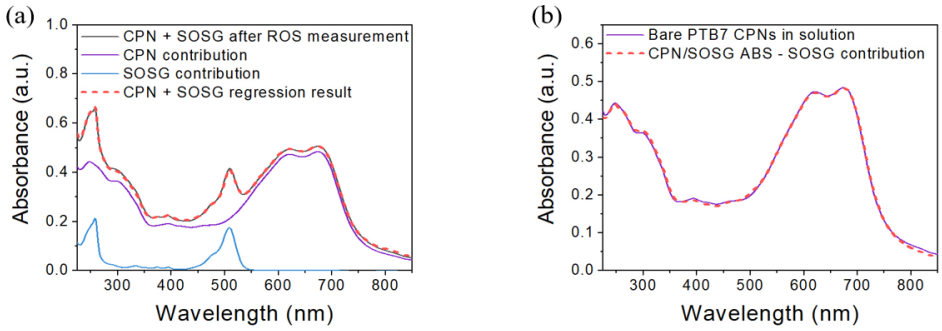


**Figure S5.5. Photochemical stability of bare PTB7 CPNs in the presence of singlet oxygen. (a)** Deconvolution of absorption spectrum of bare PTB7 CPN/SOSG mixture (black solid line) after 3 hours of continuous stimulation with 635 nm irradiation, into individual contributions from bare PTB7 CPNs (purple solid line) and SOSG (blue solid line) using regression analysis. The dashed red line shows the result of the deconvolution (R-squared value of 0.99927). Regression analysis was performed using the Multiple Linear Regression analysis functionality of Origin Pro 2018 software. **(b)** Comparison of PTB7 CPN contribution to the absorption spectrum of the CPN+SOSG mixture (red dashed line) to the absorption spectrum of bare PTB7 CPNs (purple solid line). The PTB7 contribution here is defined as the difference between the absorption of the CPN/SOSG mixture and the SOSG contribution, as determined by the regression analysis.

Using the outputs of the regression analysis, the CPN contribution to the CPN/SOSG mixture absorption can then be calculated *via* subtraction of the SOSG and background contributions:

$$A_{CPN}^{'}(\lambda) = A_{CPN+SOSG}(\lambda) - A_{bgr} - k_{SOSG}A_{SOSG}(\lambda)$$

This allowed us to compare this contribution to the original spectra of the CPN solutions (*i.e.* to compare $A_{CPN}^{'}(\lambda)$ to $k_{CPN} * A_{CPN}(\lambda)$). As shown in Figure S5.5(b) for bare PTB7 CPNs, the two spectra were nearly identical; furthermore, the CPN/SOSG solutions remained clear, homogenous and coloured throughout the singlet oxygen generation measurements. Since the absorption spectra of conjugated polymers is highly sensitive to their environment as well as chain packing, these results imply that no major chemical or structural changes occurred within the PTB7 CPNs as a result of 3-hour NIR stimulation and the resulting singlet oxygen production. That is, under the experimental conditions used, our PTB7 CPNs are resilient to photo-oxidative damage, most likely *via* efficient scavenging of the generated singlet oxygen by SOSG.

**Superoxide production**

Superoxide production by prepared PTB7 CPN samples was evaluated using the chronoamperometry method, as described in the main text of the paper. Prior to all measurements, the cell was tested on a known superoxide producer (xanthine oxide enzyme) to confirm that the electrode functioned as expected. Further control experiments were conducted to confirm 1) that the superoxide generation by the PTB7 CPNs was photoinitiated, and 2) that any changes in current measured by our cell were specific to superoxide production. To reaffirm photoinitiation, periodic irradiation with a UV source was used (Figure S6.1a): in all cases, the sizable increase in the measured current was observed when the light source was turned on (purple arrows in Figure S6.1) and a similar

decrease in the current followed when the light source was turned off (blue arrows). Note that for the PTB7 CPNs in the presence of the superoxide scavenger (superoxide dismutase, SOD), no such increase in the time-averaged current was observed (Figure S6.1a), although the amplitude and frequency of current oscillations did alter at the on/off time points. This, together with control experiments involving addition of SOD mid-way through the measurement, validates the specificity of our measurements to superoxide production by the CPNs.

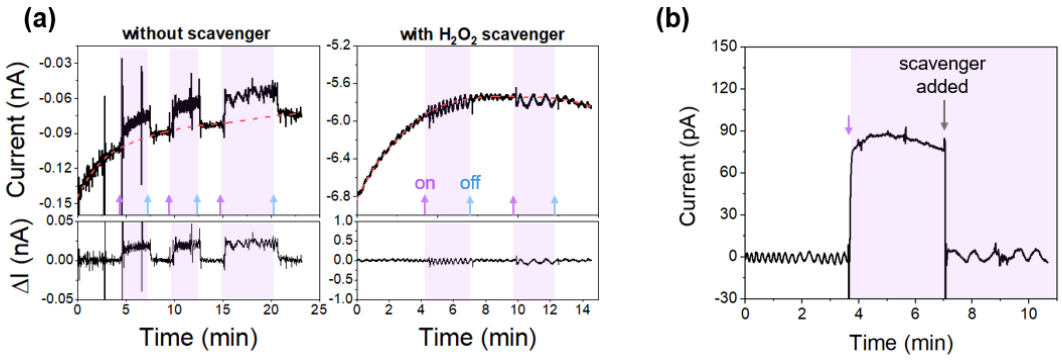


**Figure S6.1. Superoxide production by PTB7 CPNs in the presence of $H_2O_2$ scavenger. (a)** Chronoamperometry measurements on bare PTB7 CPNs in PBS, in the absence (left column) and presence (right column) of superoxide dismutase, under periodic UV irradiation. **(b)** Chronoamperometry measurements on PTB7@PSMA CPNs in PBS, under continuous UV irradiation, with the addition of superoxide dismutase at ~7 min, indicated by the grey arrow in the graph. In both panels, the UV lamp used to illuminate the cell was turned on at times indicated by purple arrows and turned off at time indicated by blue arrows, and the periods during which the UV lamp remained on are designated *via* purple shading.

According to these chronoamperometry measurements, all three types of fabricated CPNs produced approximately similar amounts of superoxide when used at high concentration of ~100 µg/mL. However, the capping of the PTB7 CPN played a crucial role in governing superoxide production by CPNs under continued illumination with UV radiation (Figure S6.2). The current dropped sharply for bare PTB7 CPNs, dropping to statistically insignificant levels within 7-10 minutes. On the other hand, chronoamperometric current remained high for both capped samples over the same period. These results are not in line with the photobleaching measurements described in Section 1, which showed approximately the same behavior for all three samples. Therefore, the superoxide itself is expected to be involved in the degradation process which leads to the decrease in the measured current, and the presence of the cap on the PTB7 CPNs affects the performance of the particle favourably.

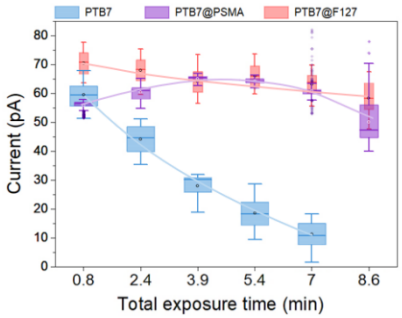


**Figure S6.2. Superoxide production by different PTB7 CPN**, as measured by chronoamperometry method. The effect of PSMA and F127 capping on superoxide production by PTB7 CPNs samples of high concentrations (90 for bare PTB7 and 100 µg/mL for PTB7@PSMA and PTB7@F127 CPNs). Non-normalized data.

**PTB7 CPNs as NIR-I imaging agents**

NIR images of 96-well plates containing fixed A549 cells previously incubated with CPNs were obtained using a customized microscopy system, as detailed in the Methods. By comparing the non-uniform distribution of cells under ambient illumination with the locations of the fluorescent CPNs, it is clear even at low magnification (10X and 20X objectives) that the CPNs trace the distribution of cells and not the zones of the well plate between cells (Figure S7.1). This co-localization is consistent with both fluorescent CPNs internalization and stable external adherence after multiple washes (see Methods).

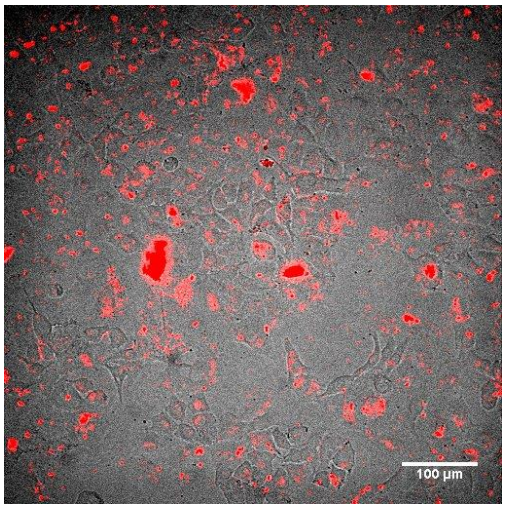


**Figure S7.1. NIR fluorescence imaging of A549 cell line incubated with PTB7@PSMA.** The fluorescence image (red) is superimposed on the ambient images (grey). Image taken with 20x objective.

Bare PTB7 CPNs as well as coated PTB7@PSMA and PTB7@F127 CPNs were incubated in duplicate wells within a 96-well plate, prior to being imaged. While the cell densities vary slightly from well to well, and from region to region in each well, they are broadly similar (Figure S7.2,

ambient images), but the fluorescence localizations are very different, showing a much larger number of fluorescence sources on the PTB7@PSMA samples than the other two. We ascribe this to an increased uptake of PTB7@PSMA compared to the other CPN formulations by the A549 cells. The fluorescence signal from the three CPN formulations is quantified in Figure S7.2(b).

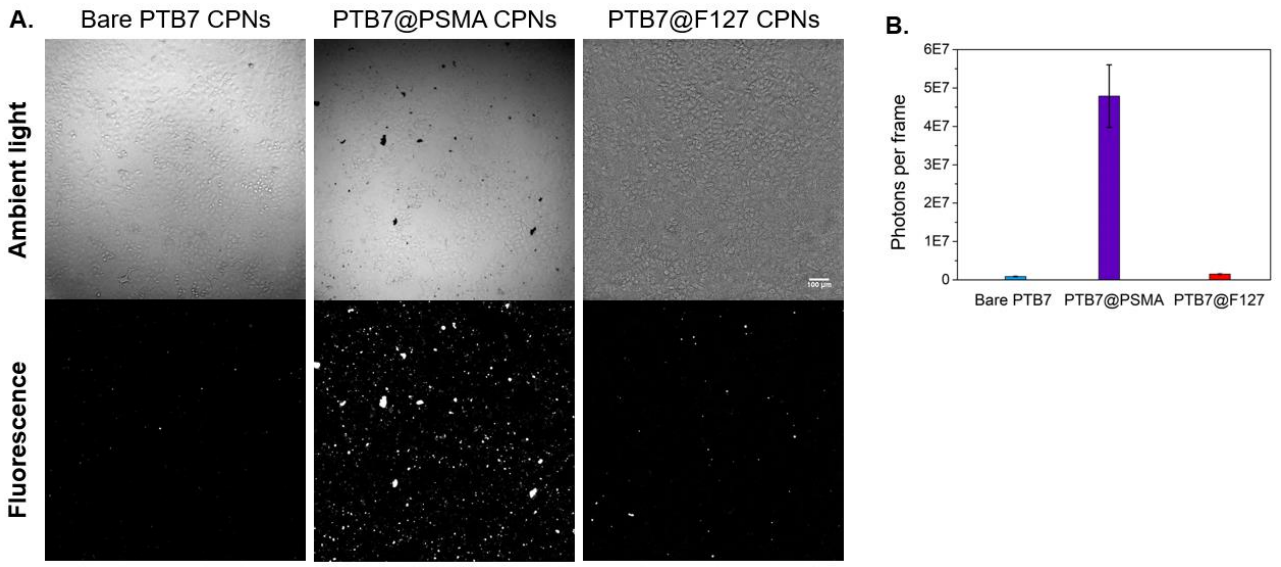


**Figure S7.2. NIR fluorescence imaging of fixed A549 cells incubated with PTB7 CPNs. A.** Figure shows ambient-light images (top row) and NIR fluorescence images (bottom row) for bare PTB7@F127 (left column), bare PTB7 (middle column) and PTB7@PSMA (right column). The illumination, camera settings and display greyscale were the same for all three fluorescent images, to ensure comparability. Images taken with 10x objective. **B.** Number of detected fluorescent photons (average per frame, above background) arising from cells incubated with stock concentrations of bare PTB7, PTB7@PSMA and PTB7@F127 CPNs, imaged through 10x objective. Error bars are standard errors, based on measurements in eight subregions across two samples.

At higher magnification (60x), the distribution of PSMA-capped CPNs within or on to the cells can be discerned (Figure S7.3). CPNs internalization is non-uniform, displaying both a low-level diffuse component consistent with local concentrations of CPNs or CPNs aggregates below the limit of resolution of the microscope. Additionally, a relatively small number of CPN aggregates are observable within the cells (consistent with vescicle mediated internalization) and non-colocalized with cells (consistent with non-internalized CPNs' un-soluble precipitates adhering to the bottom of the well).

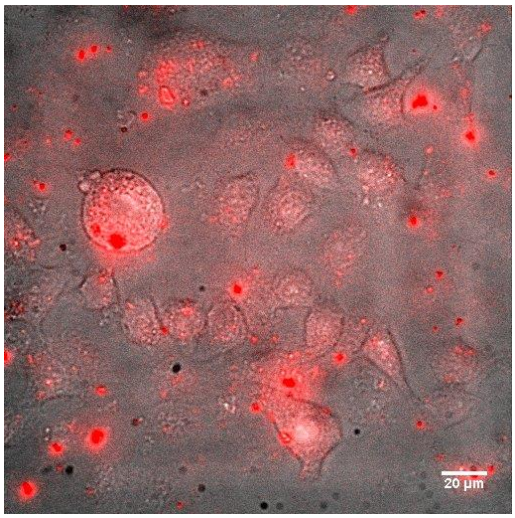


**Figure S7.3. NIR fluorescence imaging of fixed A549 cells previously incubated with PTB7@PSMA.** Fluorescent image (red) superimposed on ambient-light image (greyscale), through a 60x objective, showing in detail the non-uniform distribution of CPNs in the cells.

Cell cultures were incubated with a range of CPN concentrations, at successive dilutions by a factor of ten. Images of the PTB7@PSMA cultures over two decades of concentration (Figure S7.4) show that despite similar densities of cells (ambient images), the fluorescence signals decrease with dilution, broadly as expected. The fluorescent signal from these three CPN concentrations, and from

a fourth incubated at 1/1000th of the initial value but for which the measured fluorescence value represents the sensitivity limit of our system, is quantified in (main text) Figure 7(c).

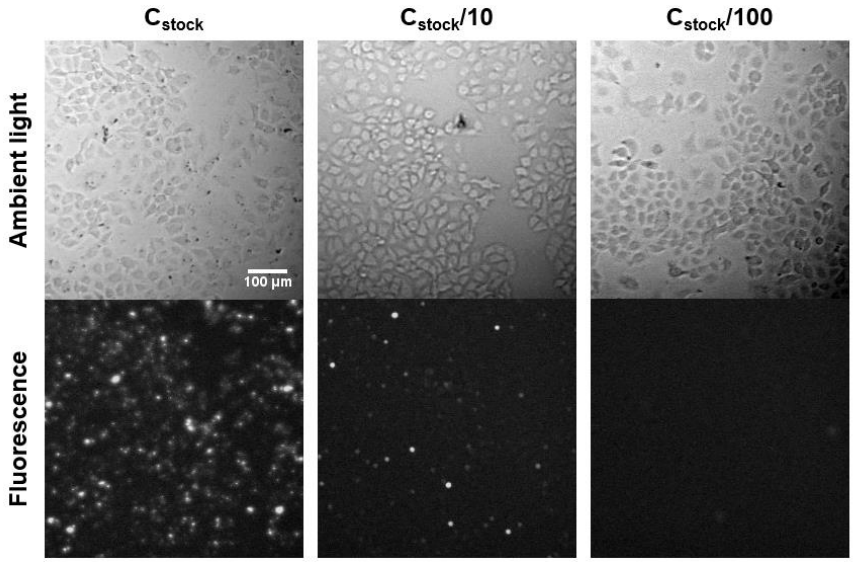


**Figure S7.4. NIR imaging of fixed A549 cell line incubated with different concentrations of PTB7@PSMA CPNs.** Ambient-light (top row) and fluorescence (bottom row) images for cells incubated with maximum concentration (left column), 1/10$^{th}$ dilution (middle column) and 1/100$^{th}$ dilution (right column) PTB7@PSMA. The illumination, camera settings and display greyscale were the same for all three fluorescent images, to ensure comparability. Images taken with 10x objective.

***In vitro* ROS production by PTB7 CPNs**

The DCFDA cellular ROS detection kit (Abcam, Cambridge, UK) was used to determine the ROS production induced by photoexcitation of CPNs, according to the manufacturer's instructions. Briefly, the cells were washed with 100 µl of 1X ROS assay buffer. The buffer was then replaced by 100 µl of DCFDA solution and incubated for 45 minutes in the dark, and then replaced by PTB7@F127 CPNs dilutions in Roswell Park Memorial Institute medium (RPMI, 0-45 µg/mL).

Without allowing time for internalisation, NIR irradiation was applied with a light dose of 10 J/cm$^2$ at 660 - 850 nm using Derma Red Lamp (Care Lamps, Care Lamps, UK) to excite the nanoparticles. Normalised fluorescence readings from the ROS-signalling DCF with an emission wavelength of 520-530 nm were taken at time intervals of 0, 30, 60 and 120 minutes (Figure S8.1a) upon incubation. Details about repeats and Positive control wells for the ROS assay were supplemented with 100μL THBP and negative control wells contained untreated cells (*n*=3). The result shows a significant increase in ROS production even with small amount of PTB7@F127 CPNs and the ROS production ability shows incubation time dependent at a higher concentration of PTB7@F127 CPNs.

To better understand the cytotoxicity of PTB7@F127 CPNs, different concentrations of PTB7@F127 CPNs with different incubation times from 0-120 min were investigated using the PrestoBlue (PB) assay (Life Technologies, Carlsbad, USA) – a commercially available, ready-to-use and water-soluble preparation. A HaCaT viability assay with PB reagent was performed according to the manufacturer's protocol. HaCaT cells were seeded in a 96-well plate at a density of $1 \times 10^4$ cells per well. Prior to the assay, the growth medium was replaced by PTB7@F127 CPNs dilutions in RPMI (Sigma-Aldrich, USA), 0-45 μg/mL. Without allowing time for internalisation, NIR irradiation was applied with a light dose of 10 J/cm$^2$ at 660 - 850 nm using Derma Red Lamp (Care Lamps, Care Lamps, UK) to excite the nanoparticles. At the end of treatment, the cells were washed with PBS and incubated with PB reagent. The viability signalling PB (resorufin) fluorescence was read (Ex/Em 560 nm/590 nm) after 0, 60 and 120 minutes. The cell viability (Figure S8.1b) was expressed as a percentage relative to the untreated cells.

All groups screened in this study showed cytotoxicity with cell viability generally lower than 5%. The cell viability did not change over the observed time period, and cell viability was not significantly affected by the increase of PTB7@F127 CPNs concentration (greater than 95% viability).

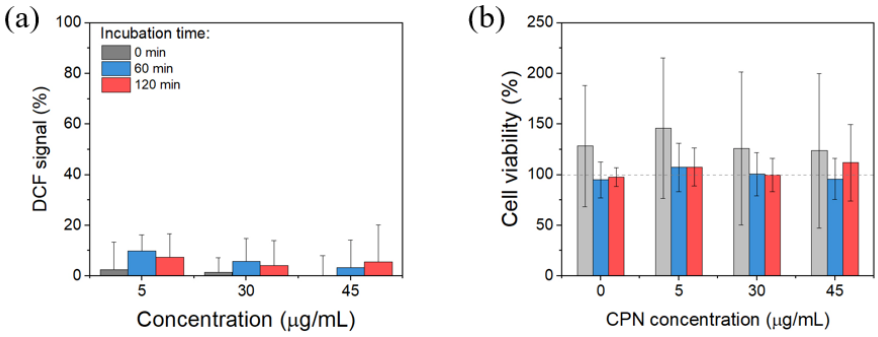


**Figure S8.1. *In vitro* ROS production by PTB7@F127 CPNs. (a)** DCF fluorescence signal and **(b)** cell viability of HaCaT cells incubated in the dark with different concentrations of PTB7 @F127 CPNs, for periods of 0 (grey), 60 (blue), and 120 (red) minutes.

**References:**

(1) Tian, G.; Sun, X.; Bai, J.; Dong, J.; Zhang, B.; Gao, Z.; Wu, J. Doxorubicin-Loaded Dual-Functional Hyaluronic Acid Nanoparticles: Preparation, Characterization and Antitumor Efficacy *in Vitro* and *in Vivo*. *Mol. Med. Rep.* **2019**, *19* (1), 133–142. https://doi.org/10.3892/mmr.2018.9687.

(2) Wang, X.; Geng, Z.; Cong, H.; Shen, Y.; Yu, B. Organic Semiconductors for Photothermal Therapy and Photoacoustic Imaging. *ChemBioChem* **2019**, *20* (13), 1628–1636. https://doi.org/10.1002/cbic.201800818.

(3) Bonnett, R.; Martinez, G. Photobleaching of Sensitisers Used in Photodynamic Therapy.

*Tetrahedron* **2001**, *57*, 9513–9547. https://doi.org/10.1002/chin.200211234.

(4) Liang, S.; Yang, X. Z.; Du, X. J.; Wang, H. X.; Li, H. J.; Liu, W. W.; Yao, Y. D.; Zhu, Y. H.; Ma, Y. C.; Wang, J.; Song, E. W. Optimizing the Size of Micellar Nanoparticles for Efficient SiRNA Delivery. *Adv. Funct. Mater.* **2015**, *25* (30), 4778–4787. https://doi.org/10.1002/adfm.201501548.

(5) Bencheikh, F.; Duché, D.; Ruiz, C. M.; Simon, J. J.; Escoubas, L. Study of Optical Properties and Molecular Aggregation of Conjugated Low Band Gap Copolymers: PTB7 and PTB7-Th. *J. Phys. Chem. C* **2015**, *119* (43), 24643–24648. https://doi.org/10.1021/acs.jpcc.5b07803.

(6) Nassar, S. J. M.; Wills, C.; Harriman, A. Inhibition of the Photobleaching of Methylene Blue by Association with Urea. *ChemPhotoChem* **2019**, *3* (10), 1042–1049. https://doi.org/10.1002/cptc.201900141.